Article

Current Biology

Dendritic architecture enables *de novo* computation of salient motion in the superior colliculus

Graphical abstract

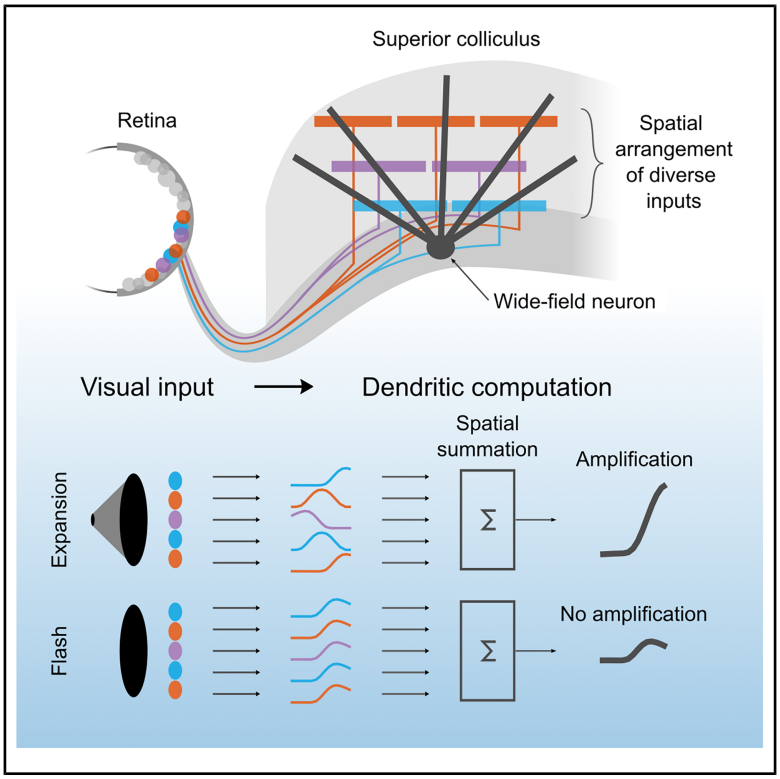

Authors

Norma K. Kühn, Chen Li, Natalia Baimacheva, Janne Zimmer, Katja Reinhard, Vincent Bonin, Karl Farrow

Correspondence

norma.kuehn@gmail.com (N.K.K.), karl.farrow@kuleuven.be (K.F.)

In brief

Kühn et al. show that the dendritic architecture of wide-field neurons in the mouse superior colliculus enables *de novo* computation of salient motion cues, with the structured integration of retinal inputs facilitating the extraction of behaviorally relevant visual features.

Highlights

- Wide-field neurons multiplex a broad set of visual motion cues
- Wide-field neurons receive retinal input from 12 functionally distinct cell types
- Retinal inputs form layered clusters along the dendrites of wide-field neurons
- Dendritic morphology is key for *de novo* computation of salient motion features

Kühn et al., 2025, Current Biology *35*, 3799–3811
August 18, 2025
https://doi.org/10.1016/j.cub.2025.06.060

CellPress

Current Biology

CellPress
OPEN ACCESS

Article

Dendritic architecture enables *de novo* computation of salient motion in the superior colliculus

Norma K. Kühn,[1,2,*] Chen Li,[1,2,3] Natalia Baimacheva,[1] Janne Zimmer,[1,2] Katja Reinhard,[1,4] Vincent Bonin,[1,2,5] and Karl Farrow[1,2,5,6,*]

[1]VIB-Neuro-Electronics Research Flanders, Herestraat 49, Leuven 3000, Belgium
[2]Department of Biology and Leuven Brain Institute, KU Leuven, Naamsestraat 59, Leuven 3000, Belgium
[3]Yale School of Medicine, 333 Cedar Street, New Haven, CT 06510, USA
[4]Scuola Internazionale Superiore di Studi Avanzati, via Bonomea 265, Trieste 34136, Italy
[5]imec, Kapelstraat 75, Leuven 3001, Belgium
[6]Lead contact
*Correspondence: norma.kuehn@gmail.com (N.K.K.), karl.farrow@kuleuven.be (K.F.)
https://doi.org/10.1016/j.cub.2025.06.060

SUMMARY

Dendritic architecture plays a crucial role in shaping how neurons extract behaviorally relevant information from sensory inputs. Wide-field neurons in the superior colliculus integrate visual information from the retina to encode cues critical for visually guided orienting behaviors. However, the principles governing how these neurons filter their inputs to generate appropriate responses remain unclear. Using viral tracing, two-photon calcium imaging, and computational modeling, we show that wide-field neurons receive functionally diverse inputs from 12 retinal ganglion cell types, forming a layered, type-specific organization along their dendrites. This structured arrangement allows for wide-field neurons to multiplex salient motion cues, selectively amplifying movement and suppressing static features. Computational models reveal that the spatial organization of dendrites and inputs enables the selective extraction of behaviorally relevant stimuli, including *de novo* computations. Our findings underscore the critical role of dendritic architecture in shaping sensory processing and neural circuit function.

INTRODUCTION

Dendrites provide a spatial dimension to neural computations, extending processing beyond temporal integration at the soma. Their inputs are precisely organized to align dendritic branches with inputs from specific brain regions, cell types,[1–4] or retinotopic locations.[5–8] These spatial arrangements dictate where inputs arrive on the dendrite and how they are shaped by its electrical properties, supporting both linear and nonlinear computations such as band-pass filtering[9,10] and nonlinear summation.[11–14] Studies of local circuits in the retina have linked dendritic structure and the arrangement of inputs to specific computations of defined cell types.[15–17] However, how these factors shape computations as information is passed to central brain regions remains poor, largely owing to limited knowledge of the relationship between specific inputs[1,18] and dendritic structure.[19,20] Here, we demonstrate that dendritic architecture and arrangement of inputs enable a *de novo* computation of salient motion cues in neurons of the mouse superior colliculus (“colliculus”).

The colliculus plays a central role in detecting salient visual stimuli that guide ongoing behavior. Here, we define “saliency” as those visual features (e.g., motion and contrast) that preferentially trigger innate orienting and avoidance responses, including approach, freezing, and escape. In the colliculus, these features are often tied to object motion,[21–23] enabling mice to rapidly detect approaching threats or fleeing prey.[24,25] Neurons in the colliculus integrate inputs from ~40 retinal ganglion cell types,[26–28] each encoding distinct visual attributes, e.g., motion, contrast, or orientation, to guide innate behaviors, including predator avoidance and prey capture.[24,25,29,30] A central question is whether the colliculus merely relays visual inputs from the retina or actively computes new features. Its retinotopic organization preserves the spatial relationship of inputs to form a detailed map of the visual field.[7,31,32] Additionally, the specific depth at which retinal inputs arrive in the optic layers[2,31,33,34] indicates that neurons could selectively sample inputs by depth. Recent evidence suggests that the colliculus selectively filters specific features to generate saliency maps, rather than simply inheriting them.[31,35–38]

We investigated how genetically targetable wide-field neurons of the colliculus process and refine their retinal inputs to encode behaviorally relevant information. Wide-field neurons derive motion saliency[39,40] from a specific set of retinal ganglion cell types[41] to drive freezing and hunting behaviors (Figure 1A).[25,42–44] Using viral tracing, two-photon calcium imaging, and patch-clamp recordings, we mapped their inputs and outputs in response to visual stimuli. We found that their unique dendritic structure and spatial distribution of inputs enable multiplexing of salient motion cues. While some retinal ganglion cells exhibit strong selectivity for looming stimuli,[45] representation of receding motion emerges *de novo* within the colliculus. Computational modeling revealed that the summation of retinotopically organized inputs across the dendritic tree is key to

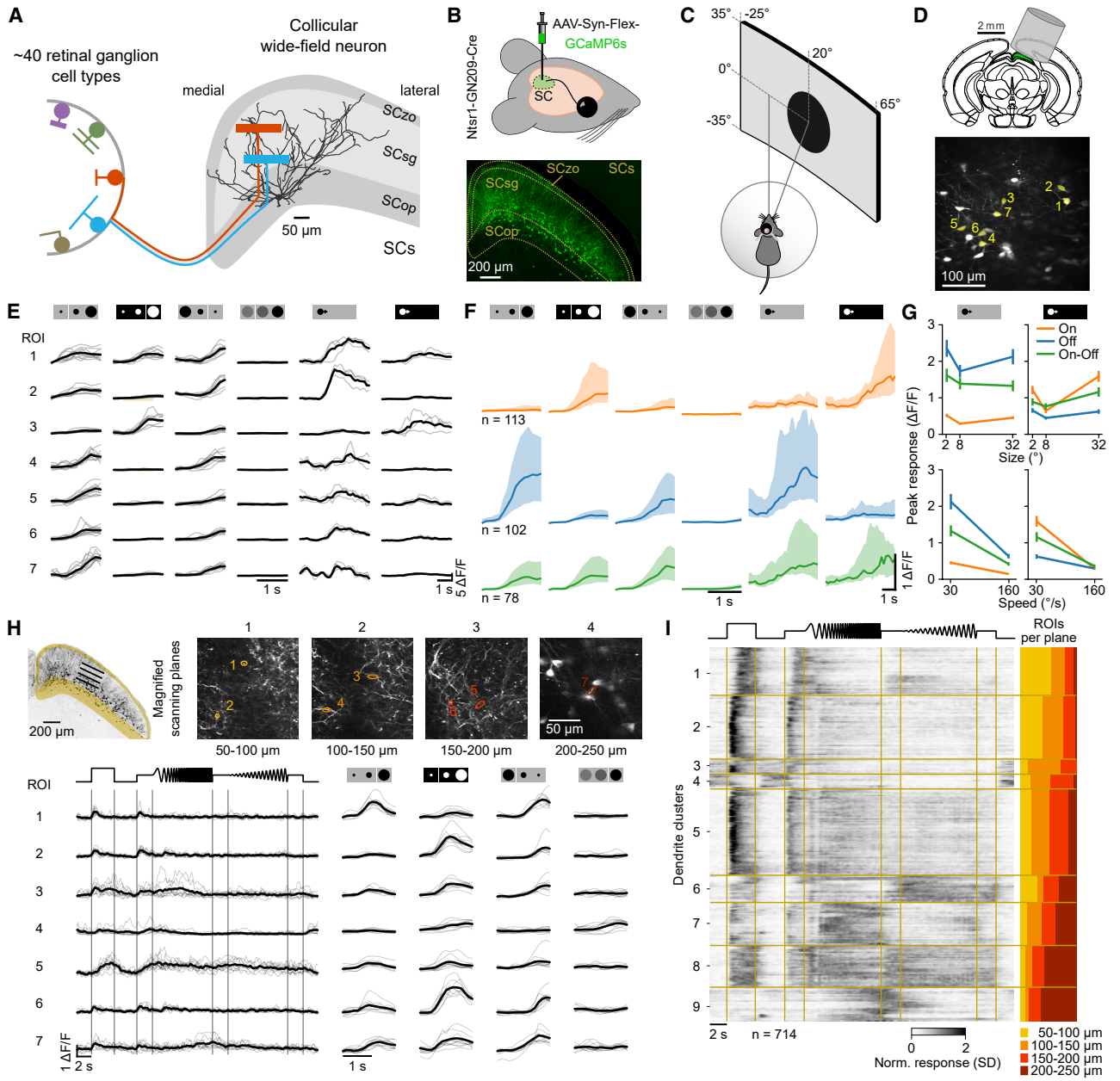

Figure 1. Characterization of visual responses of wide-field cell bodies and dendrites

(A) Schematic of wide-field neurons of the colliculus and type-specific layered input from retinal ganglion cells. SCzo, zonal layer; SCsg, superficial gray layer; SCop, optic layer of the sensory-related colliculus (SCs).

(B) Viral labeling of wide-field neurons in Ntsr1-GN209-Cre mice.

(C) *In vivo* two-photon calcium imaging setup. Visual stimuli were presented at 0° elevation and 20° azimuth in front of the contralateral eye.

(D) Position of the cranial window for two-photon imaging (top) and example field of view (bottom).

(E) Wide-field neuron cell body responses; individual trials shown in gray, median response in black. Cell body locations indicated in (D). Visual stimuli from left to right: black and white expanding disk, black shrinking disk, dimming disk, and large and slow sweeping disks in black and white.

(F) Median responses of clustered On-, Off-, and On-Off-type wide-field cell bodies to expanding, shrinking, dimming, and large, slow sweeping disks. Shaded area indicates IQR.

(G) Mean peak responses of On, Off, and On-Off types to black and white sweeping stimuli. Upper: size tuning at 30°/s speed. Lower: speed tuning at 32° disk size. Error bars indicate standard deviation. Data from 12 mice across 13 sessions (293 cell bodies).

(H) Scanning planes for volumetric imaging (top) and example dendritic region of interest (ROI) responses across all scanning planes (bottom). Scanning planes magnified ×2; ellipses indicate ROIs.

(I) Heatmap of normalized and clustered dendritic responses to a full-field stimulus (left) and depth profiles of identified clusters (right), sorted by mean cluster depth. Data from 18 mice across 22 sessions (714 ROIs).

See also Figure S1.

these computations, demonstrating that spatially organized dendritic computations underpin motion saliency processing in the colliculus.

RESULTS

Wide-field neurons multiplex motion signals and exhibit diverse contrast preferences

We investigated the role of dendrites in wide-field neuron encoding of salient stimuli in three steps: (1) recording the responses of wide-field neurons and dendritic compartments, (2) identifying the visual features relayed by innervating retinal ganglion cells, and (3) determining the key components required to transform inputs into outputs using computational models incorporating dendritic properties. We assessed the visual features encoded by wide-field neurons by recording their responses to visual stimuli in head-fixed, behaving mice by using two-photon calcium imaging (Figure 1). A calcium indicator was expressed using a Cre-dependent adeno-associated virus (AAV-Syn-Flex-GCaMP6s) injected into the left colliculus of *Ntsr1-GN209 Cre* mice (Figure 1B). Visual stimuli were presented to the contralateral eye, while mice were free to run on a floating ball (Figure 1C). Neurons were imaged through a cannula window, implanted above the anterior two-thirds of the colliculus (Figure 1D).

We found that wide-field neurons respond to a diverse set of moving stimuli but showed minimal responses to static stimuli (Figure 1E). To characterize their response properties, we presented expanding, shrinking, and sweeping black disks, as well as dimming disks on a gray background. Disks were linearly expanding or shrinking with an edge speed of 30°/s, while sweeping disks were presented in three sizes (2°, 8°, and 30°) and two speeds (30°/s and 160°/s). Expanding and sweeping disks were also shown in reverse contrast. Calcium responses were recorded from wide-field neuron cell bodies at 200–250 μm below the surface of the colliculus (Figures 1D and 1E). They exhibited diverse contrast preferences, with some neurons responding only to black moving disks and others only to white disks (Figure 1E). Responses were strongest to slowly moving edges, as indicated by comparable peak responses to expanding, shrinking, and slowly sweeping disks. Peak responses to white expanding, black shrinking, and black and white slowly sweeping disks, computed from responses normalized by the standard deviation (SD) across stimuli, were compared with those elicited by black expanding disks (median [interquartile range (IQR)] difference in SD: −0.05 [−0.27, 0.18], −0.08 [−0.26, 0.07], 0.11 [−0.13, 0.31], −0.15 [−0.36, 0.04]; p values 0.48, 0.28, 0.14, 0.34, Kruskal-Wallis test). In contrast, responses were significantly weaker for dimming disks and fast black and white sweeping disks (median [IQR] difference: −0.61 [−0.76, −0.49], −0.43 [−0.60, −0.28], −0.44 [−0.61, −0.31]; p values 10^{-38}, 10^{-10}, 10^{-9}, Figure S1). These results show the selective encoding of slowly moving edges, enabling wide-field neurons to act as multiplexers of slow motion cues.

We identified three functional types: On, Off, and On-Off cells, based on clustering and contrast preference to expanding, shrinking, and dimming disks (Figure 1F; see also Figure S1). Each type responded strongly to expanding, shrinking, and sweeping disks of their preferred contrast but not to the dimming disk where no moving edge was present (Figures 1F and 1G). On and Off types showed significantly stronger peak responses to an expanding disk of their preferred contrast, compared with an expanding disk of their unpreferred contrast (median [IQR] difference of peaks: On: 1.7 [1.4, 1.9] SD, Off: 1.3 [1.0, 1.6] SD, p values 10^{-21} and 10^{-25}, Kruskal-Wallis test), while On-Off cells did not show statistically significant differences between On and Off contrasts ($p = 0.09$). Wide-field neurons preferred slow sweeping disks (30°/s) over fast sweeping disks (160°/s), indicated by their peak responses (median [IQR] differences of peaks between slow and fast: 0.55 [0.41, 0.72], 0.23 [0.14, 0.35], and 0.32 [0.25, 0.39] for black and 0.09 [0.06, 0.16], 0.01 [−0.02, 0.05], and 0.22 [0.15, 0.43] for white disks of sizes 2°, 8°, and 32°, p values 10^{-18}, 10^{-9}, 10^{-14}, 0.06, 0.42, 10^{-12}, Wilcoxon signed-rank; Figure 1G). The preference for slow speeds of sweeping disks is in line with the ratio of wide-field neurons' preferred spatial and temporal frequencies that peak at 2 Hz and 0.04/°, respectively, resulting in a preferred speed of ∼30°/s (Figure S1). This suggests that wide-field neurons are finely tuned to process slow motion signals critical for detecting environmental changes, such as the movement of predators or prey, with their selective encoding emphasizing the saliency of slow motion cues.

Depth-dependent clustering of dendritic visual responses

Retinal inputs to the colliculus are organized in distinct functional and depth-specific clusters.[2,33] A key question is whether wide-field neuron dendrites maintain the layered organization of retinal inputs, potentially enabling compartmentalized processing of visual information. To investigate this, we additionally presented a full-field stimulus with rich temporal dynamics but no moving edges[18,26] and recorded dendritic calcium responses quasi-simultaneously across four scanning planes, from the collicular surface to the cell bodies (Figure 1H). The stimulus evoked highly localized responses in dendrites (Figure 1H; see also Figure S1).

Clustering dendritic responses revealed nine distinct functional groups (Figure 1I). Seven clusters exhibited On-type responses to the transition from black to white, while only clusters 3 and 4 showed Off-type responses with sustained activity when the screen turned black. The clusters also differed in temporal frequency preference, with most responding to low frequencies (clusters 1–6), whereas clusters 7 and 8 were tuned to higher frequencies.

These functional clusters were organized by depth, suggesting a functional compartmentalization of the dendrites. Sorting clusters by the mean depth of their signals revealed a characteristic depth profile (Figure 1I, right): clusters 1 and 2 occupied the most superficial layers (50–150 μm), clusters 3 and 4 were found at intermediate depths (100–200 μm), clusters 5–7 spanned all scanning planes, and clusters 8 and 9 were restricted to the deepest layers (150–250 μm). Noise correlation analysis revealed that approximately one-third of dendritic compartments were strongly correlated with the soma of a nearby wide-field neuron ($r > 0.7$). Among these, individual neurons typically exhibited dendritic compartments with diverse functional tuning profiles, spanning multiple (up to six) of the previously defined functional clusters. This functional heterogeneity within single neurons supports the idea that dendritic responses reflect local, compartmentalized integration of retinal inputs. Together, these findings suggest

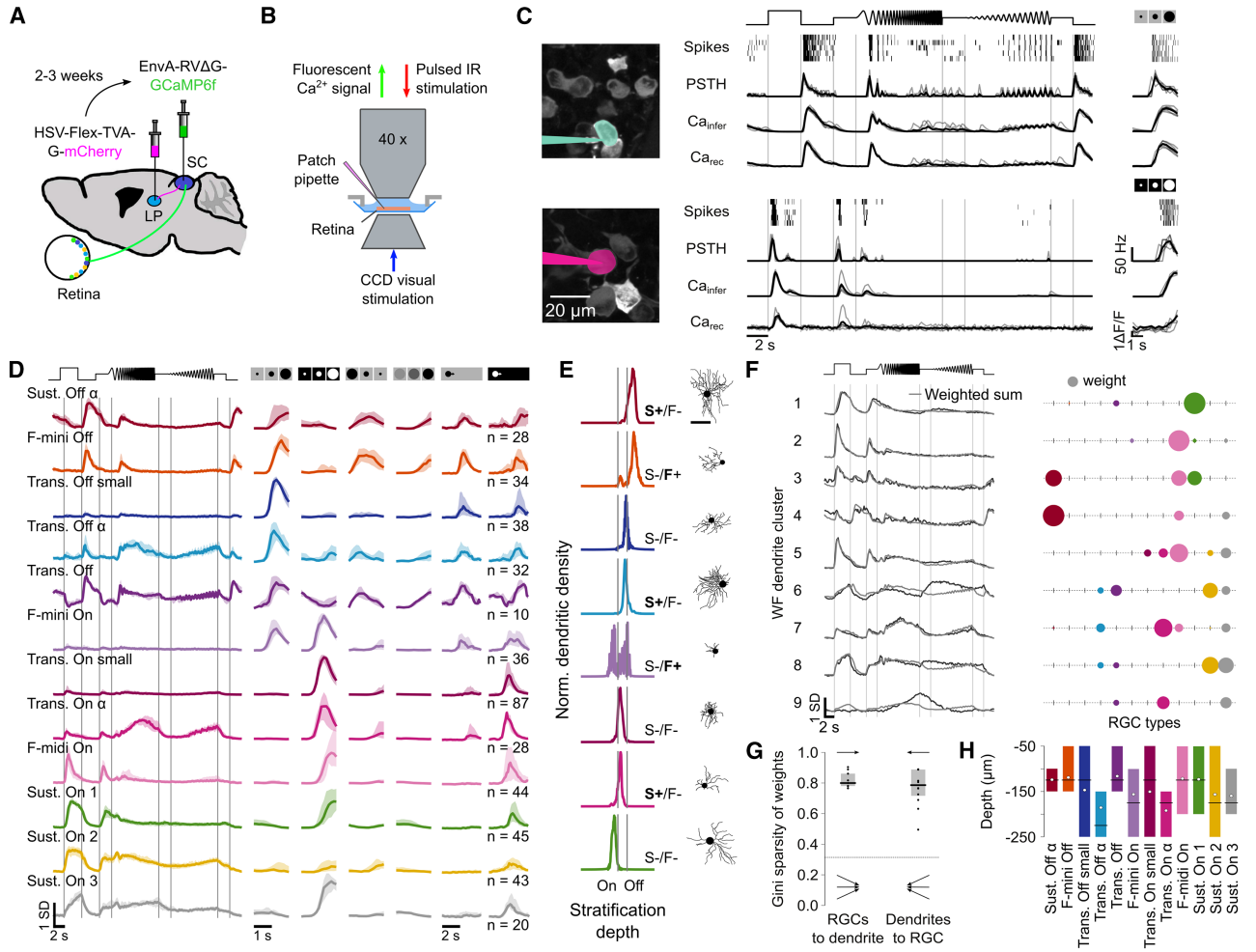

Figure 2. Twelve retinal ganglion cell types provide input to wide-field neurons

(A) Viral strategy to label retinal ganglion cells innervating wide-field neurons. Retrograde helper virus (HSV-Flex-TVA-G-mCherry, magenta) was injected into the lateral posterior nucleus of the thalamus (LP) and rabies virus (EnvA-RVΔG-GCaMP6f, green) into the colliculus (SC).

(B) *Ex vivo* recordings of labeled retinal ganglion cells using two-photon calcium imaging and whole-cell patch-clamp recordings.

(C) Spiking responses, peristimulus time histogram (PSTH), inferred calcium signal, and simultaneously recorded calcium signals of a sustained Off alpha cell (top) and a transient On alpha cell (bottom), individual trials shown in gray, median response in black.

(D) Normalized responses of identified retinal ganglion cell clusters (lines, median; shaded areas, IQR). Data from 24 mice (445 retinal ganglion cells).

(E) Examples of morphologically and molecularly identified retinal ganglion cell types, color-matched to clusters in (D). S±, SMI32 positive or negative; F±, FOXP2 positive or negative; scale bar 100 μm.

(F) Weighted sum of retinal ganglion cell types to match full-field stimulus responses of wide-field neuron dendrites. Left: weighted sum (gray) to match median response of each dendritic cluster (black). Right: weights of each retinal ganglion cell type. Disk color and size indicate cell type and weight, respectively.

(G) Gini sparsity of weights of retinal ganglion cell types to wide-field dendrite or wide-field dendrites to retinal ganglion cell type. Thick horizontal lines and gray boxes indicate median and IQR. Individual data points in black. Dashed horizontal line indicates Gini sparsity of uniformly distributed weights.

(H) Depth distribution of retinal ganglion cell inputs in the colliculus, determined by the most strongly correlated dendritic signals of wide-field neurons. White dots, horizontal lines, and boxes indicate mean, median, and IQR of each ganglion cell type.

See also Figures S2 and S4.

that wide-field neuron dendrites receive depth-specific input from distinct retinal ganglion cell types, supporting parallel processing of visual features within separate dendritic compartments.

Twelve retinal ganglion cell types relay diverse visual features to wide-field neurons

To identify the retinal ganglion cells that provide input to wide-field neurons, we used rabies-based transsynaptic retrograde tracing to label innervating retinal ganglion cells (Figure 2A).[41] Labeled cells were recorded *ex vivo* using two-photon calcium imaging or whole-cell patch-clamp recordings while visual stimuli, identical to those presented to wide-field neurons, were projected onto the retina (Figures 2B and 2C). To ensure consistency in the dataset and facilitate comparison with calcium signals in wide-field neurons, spiking activity from patch-clamp recordings was converted to calcium signals by convolving with a GCaMP6s kernel (rise time: 0.1 s, decay time: 0.4 s). Examples of simultaneously recorded spiking and calcium activity,

along with convolved signals, are shown in Figure 2C (see also Figure S2). To classify the recorded retinal ganglion cells, based on molecular and structural features, a subset of cells was stained for key molecular markers of major retinal ganglion cell types (Smi32, Foxp2, Cart), and their dendritic arbors were reconstructed (Figure S2).

Retinal ganglion cell calcium responses were grouped using agglomerative clustering with subsequent manual curation, leading to 12 functional types: 5 Off, 1 On-Off, and 6 On types (Figure 2D). Clusters were matched to existing cell types from previous studies[26,27,41] by using a subset of molecularly and morphologically identified cells (Figure 2E; see also Figure S2).

The identified On, Off, and On-Off retinal ganglion cell types exhibit distinct response profiles to full-field flashes and expanding disks of corresponding contrast. On types respond significantly more strongly to On flashes and expanding white disks, compared with Off flashes and expanding black disks, while Off types show the reverse pattern. On-Off types respond to both black and white expanding disks, indicating sensitivity to both contrast polarities. In addition to their responses to expanding black disks, four of the five Off cell types also responded to shrinking and dimming disks, although with lower amplitudes (median [IQR] differences of peaks −0.32 [−0.4, −0.2] and −0.57 [−0.67, −0.47] SD, p values 0.002 and 10^{-21}, Kruskal-Wallis test). This response profile contrasts with that of wide-field neuron cell bodies, where all three types showed strong responses to shrinking black disks but did not respond to dimming disks (Figure 1F). These differences suggest that wide-field neurons integrate retinal inputs in a manner that selectively amplifies specific motion cues while filtering out luminance changes.

Retinal ganglion cells provide layered, type-specific input to wide-field neuron dendrites

To determine whether the diverse response profiles observed in wide-field neuron dendrites can be explained by the retinal inputs, we fitted a linear regression model with non-negative matrix factorization (NNMF) to the full-field stimulus responses of each wide-field dendrite cluster as a weighted sum of the 12 retinal ganglion cell types. The positively constrained weights reflect the excitatory nature of retinal inputs. This approach produced reasonable fits and a sparse weight matrix (Figures 2F and 2G). Responses in the upper dendrites were well reconstructed by the linear model (Figure 2F, clusters 1–5 and 7), whereas responses in the lower dendrites showed poorer fits (clusters 6, 8, and 9). This suggests that summation closer to the cell body may involve additional integration mechanisms.

The fitted weights reveal that each dendritic signal can be accounted for by only a few retinal ganglion cell types (Figure 2F). To quantify the convergence and divergence of retinal inputs onto wide-field dendrites, we calculated the Gini sparsity index (Figure 2G). High values (0.81 [0.78, 0.86] for retinal ganglion cell-to-dendrite connections and 0.77 [0.72, 0.83] for dendrite-to-retinal ganglion cell connections) indicate sparse, highly specific connectivity, significantly deviating from a uniform distribution (p values 10^{-38} and 10^{-21}, respectively, Mann-Whitney U test; Figure 2G). This further supports functional compartmentalization, where each local dendritic signal is shaped by only a few retinal ganglion cell types. Correlating retinal signals with dendritic signals to determine their innervation depth, revealed that retinal ganglion cell types map onto specific dendritic locations within the colliculus (Figure 2H). These findings demonstrate that retinal inputs are organized in a layered, type-specific manner along wide-field neuron dendrites, supporting functional compartmentalization.

Wide-field neurons perform a *de novo* computation of responses to shrinking disks

Unlike dendritic signals, cell body responses cannot be reconstructed by a weighted sum of retinal inputs. To test whether they fit a linear model with non-negative weights, we reconstructed responses to both contrasts of expanding disks, as well as shrinking and dimming disks (Figure 3A). The fitted weights indicate that each wide-field neuron type receives input from a limited set of retinal ganglion cell types. On and Off wide-field neurons appear to be driven by largely distinct sets of retinal inputs with opposite weight distributions, while On-Off wide-field neurons share input with both On and Off types (Figure 3B; see also Figure S3). Notably, while responses of the On type were well matched by the linear model, the model failed to capture the responses of the Off and On-Off type to a shrinking disk (Figure 3C).

To quantify the discrepancy between peak amplitudes of measured and fitted responses, we calculated the pairwise difference of peaks for each wide-field neuron. The distribution of these differences revealed a systematic underestimation of peak responses to the shrinking stimulus especially in Off and On-Off types. A similar trend was observed when calculating the mean squared error for each stimulus type (Figure 3D; see also Figure S3).

Since the response amplitude of wide-field neurons to shrinking stimuli is consistently underestimated by the weighted sum of retinal inputs, we asked whether the strong responses reflect a *de novo* computation within wide-field neurons. Retinal ganglion cells showed stronger responses to expanding stimuli, suggesting that the enhanced shrinking responses in wide-field neurons may emerge within the colliculus. To test this, we computed an expansion selectivity index based on peak responses for each retinal ganglion cell and wide-field neuron and compared their distributions (Figure 3E). This revealed a shift in stimulus preference: while retinal ganglion cells preferred expanding over shrinking stimuli (expansion selectivity index: 0.17 [−0.26, 0.46]), wide-field neurons responded similarly to both (expansion selectivity index: 0.02 [−0.26, 0.27]) with significant difference from the retinal distribution ($p = 10^{-4}$, Mann-Whitney U). Furthermore, wide-field neurons exhibited a stronger preference for expanding over dimming stimuli (0.54 [0.17, 0.83]), compared with retinal ganglion cells (0.31 [0.01, 0.70], $p = 10^{-6}$, Mann-Whitney U).

Inhibition from collicular interneurons does not improve response predictions

Wide-field neurons receive local inhibition from GABAergic interneurons of the colliculus.[29] To test whether local inhibition can account for wide-field neurons' enhanced responses to shrinking stimuli, we measured the calcium responses of *Gad2*-positive neurons of the colliculus to full-field, expanding, shrinking, and dimming stimuli (Figures 4A and 4B). Clustering revealed four distinct response types (Figure 4B; see also Figure S4). Types 1 and 2 responded most strongly to the full-field stimulus,

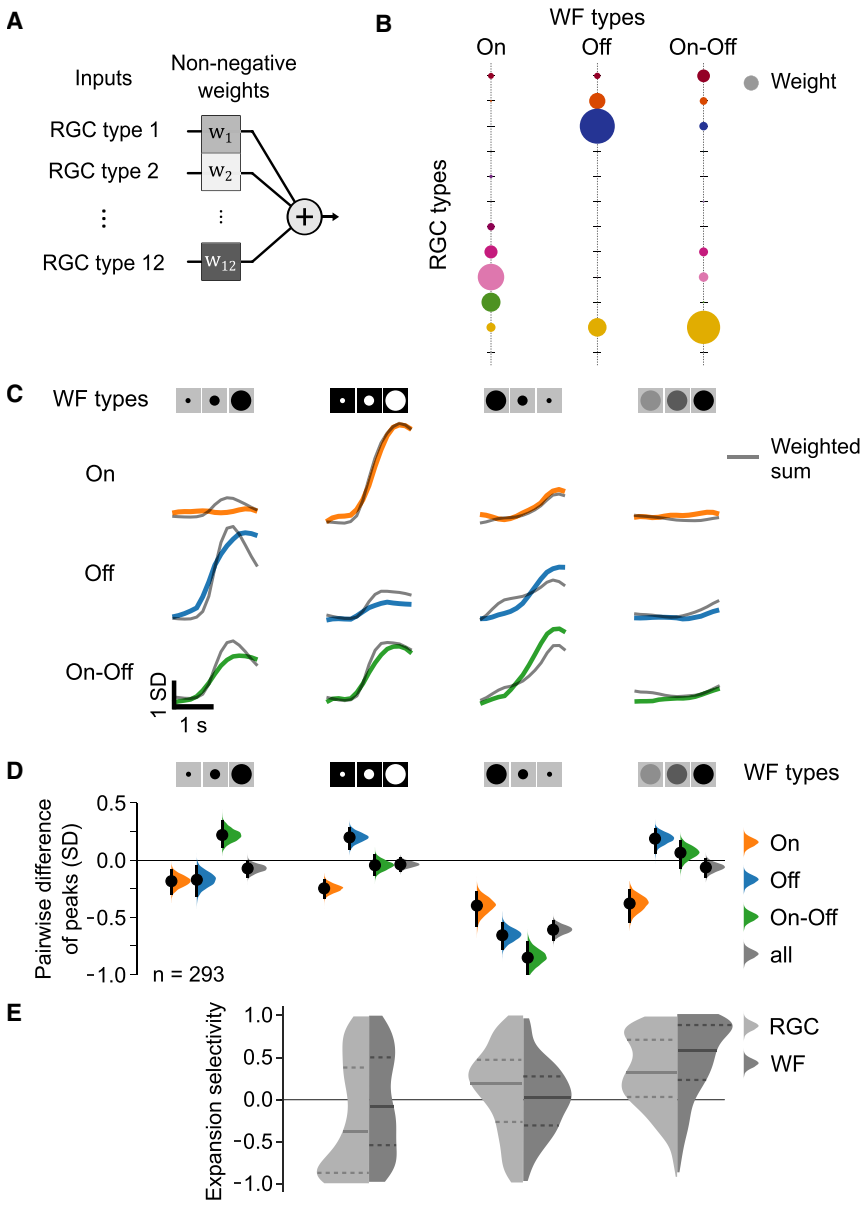

Figure 3. A linear point neuron model underestimates wide-field neuron responses to shrinking stimuli

(A) Non-negative linear regression model predicting wide-field neuron cell body responses from retinal ganglion cell inputs.

(B) Fitted weights for each retinal ganglion cell type, indicating their contribution to wide-field neuron types.

(C) Mean linear model fits (gray) overlaid on measured responses (colored) for the three wide-field neuron types.

(D) Peak response differences between measured and fitted responses for each wide-field neuron type. Dots and error bars indicate the mean and 95% confidence interval of the resampled distribution.

(E) Expansion selectivity index distributions for retinal ganglion cells (light gray) and wide-field neurons (dark gray). An index of 1 indicates a strong preference for black expanding disks. Horizontal and dashed lines represent the median and IQR, respectively. Data as in Figures 1 and 2. See also Figure S3.

whereas types 3 and 4 were broadly activated by all stimuli, with a slight preference for On-type stimuli, e.g., the white expanding disk and the On component of the full-field stimulus.

To incorporate inhibition into our model, we sign inverted the *Gad2* neuron responses while maintaining non-negative weights, as in the previous model (Figure 4C). This revealed that inhibition primarily originated from *Gad2* types 1 and 2, which contributed to both somatic and dendritic signals of wide-field neurons (Figure 4D; see also Figure S4). In particular, reconstructions of Off-type wide-field neurons included inhibitory input from type 1 and a smaller contribution from type 2 *Gad2* neurons. This primarily increased the contribution of inputs from sustained Off alpha cells, counteracting the inhibition. When fitting the responses of wide-field neuron dendrites, type 1 inhibition contributed more prominently to signals in lower dendritic regions, while type 2 influenced signals in upper dendritic regions (Figure S4).

Even with inhibitory inputs included, the model still underestimated wide-field neuron responses to shrinking stimuli (Figure 4E). While inhibition may shape dendritic processing, it alone does not account for the strong somatic responses to shrinking stimuli.

Complex multilayer models with nonlinear integration offer marginal improvements

To assess the role of nonlinear processing, we implemented a fully connected multilayer perceptron (MLP) that incorporated excitatory and inhibitory summation, as well as nonlinear dendritic and somatic processing. A sigmoidal nonlinearity was applied to model supralinear and sublinear integration along the dendrites, while the spiking threshold at the soma was captured using a rectifying nonlinearity at the output layer (Figure 5A; see also Figure S5).

While increasing model complexity enhances fit quality, nonlinear multilayer models provide only limited gains in predicting wide-field neuron responses. We fitted models of varying complexity, from one to three layers and L1 regularization to control sparsity of weights. The simplest model, which only included a rectifying nonlinearity, showed negligible improvement, whereas additional layers progressively enhanced fit accuracy when considering the average response (Figure 5B). To specifically evaluate model performance on the shrinking stimulus, we analyzed the difference of peaks between observed and predicted responses (Figure 5C). Increasing model complexity gradually reduced this difference, with significant improvements in two-layer

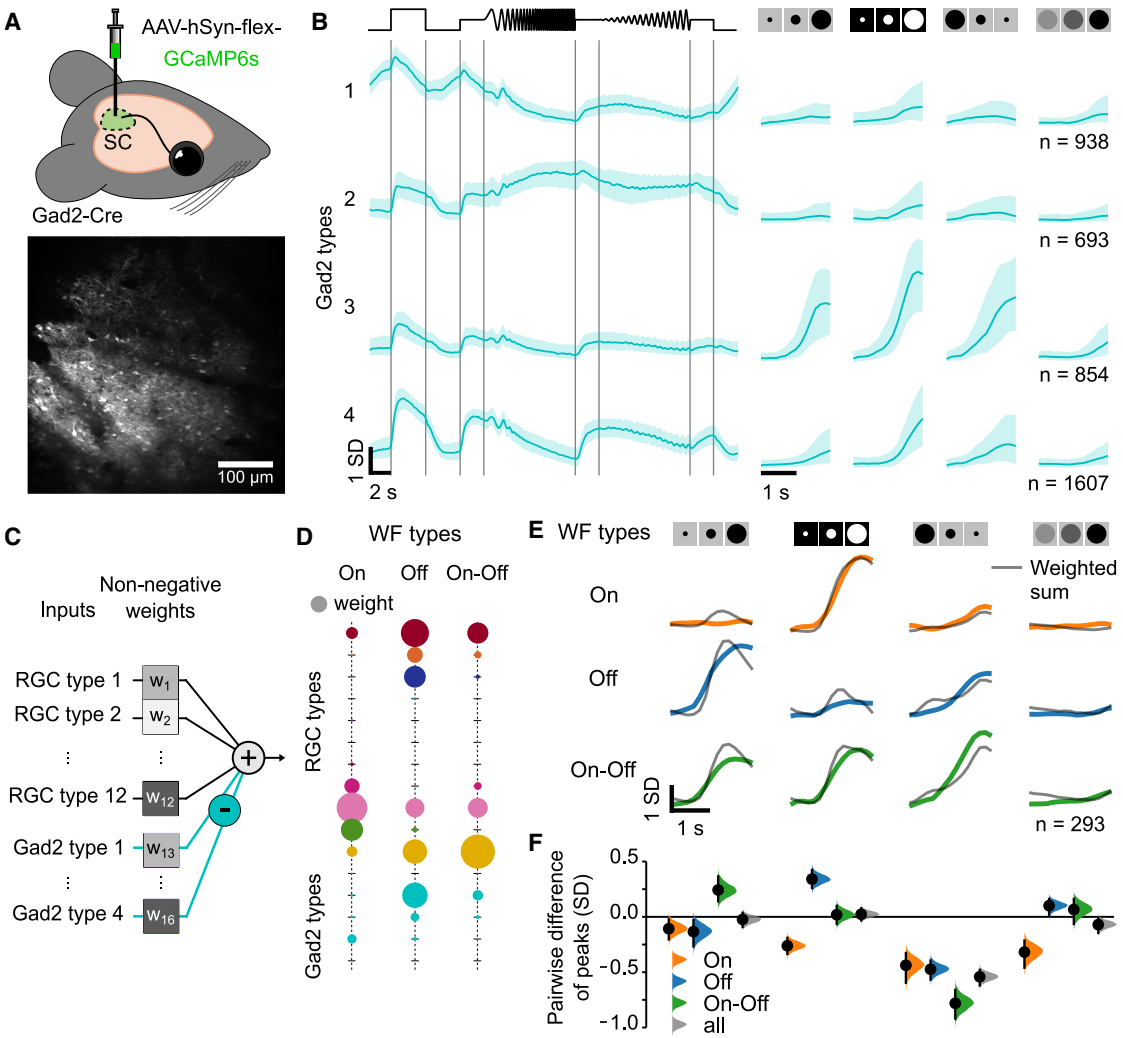

Figure 4. Accounting for inhibition from GABAergic neurons in the colliculus provides only marginal improvement to the linear model

(A) Labeling of Gad2-positive neurons in the colliculus (SC) and an example field of view from *in vivo* two-photon imaging.

(B) Median and IQR of normalized responses from four Gad2 neuron clusters to full-field, expanding, shrinking, and dimming stimuli. Data from 4,096 neurons across 22 sessions from 12 animals.

(C) Extended linear model incorporating inhibition, with responses of Gad2 clusters sign inverted to reflect their inhibitory effect.

(D) Fitted weights indicating the contribution of retinal ganglion cell and Gad2 neuron types to each wide-field neuron type.

(E) Weighted sum (gray) overlaid on measured wide-field neuron responses (colored).

(F) Pairwise difference of peaks between fitted and measured responses. Dots and error bars indicate the mean and 95% confidence interval of the resampled distribution.

See also Figure S4.

models containing five hidden nodes and three-layer models with five plus two hidden nodes. However, these models required a high number of parameters and dense weight matrices, performing best only when regularization was minimal (see also Figure S5). This suggests that additional, potentially linear mechanisms must be considered to fully explain wide-field neuron responses.

Retinotopic input organization along dendrites best predicts wide-field neuron responses

Two models, each based on distinct passive dendritic properties, can account for the *de novo* computation observed in wide-field neurons. In the first, passive dendrites act as low-pass filters, introducing temporal delays for inputs arriving at distal dendrites, compared with those near the soma (Figure 6A). In the second, the retinotopic arrangement of inputs along the dendrites gives rise to a cumulative activation of inputs during stimulus motion (Figure 6B). To capture these effects, we implemented two corresponding models by adding filtered input components, effectively doubling the number of parameters.

First, we examined the impact of dendritic filtering. We applied low-pass filters with five different cutoff frequencies (3.5, 2.5, 1.5, 0.5, and 0.35 Hz, inducing temporal delays of 0.03, 0.1,

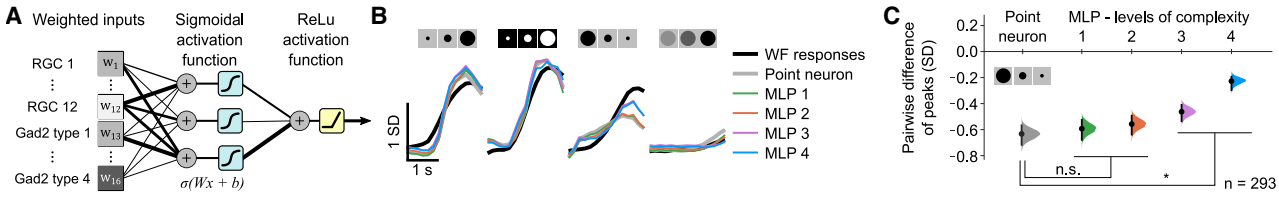

Figure 5. A multilayer model with nonlinearities improves fit at the cost of complexity

(A) MLP model incorporating retinal and inhibitory inputs, with sigmoidal activation functions in hidden layers and a rectifying nonlinearity at the output layer.

(B) Mean wide-field cell body responses (colored), with linear fits (black) and MLP fits of increasing complexity: (1) single-layer model with a rectifying output, (2) two-layer model with three hidden sigmoidal nodes, (3) two-layer model with five hidden sigmoidal nodes, (4) three-layer model with five and two hidden nodes in the first and second layers, respectively.

(C) Model performance comparison based on the pairwise difference of peaks of wide-field neuron responses and fits for the shrinking stimulus, across models described in (B). Dots and error bars indicate the mean and 95% confidence interval of the resampled distribution. *P* values in comparison with point neuron model: 0.97, 0.97, 0.045, and 0.004 for MLP models 1-4, Mann-Whitney U test.

See also Figure S5.

0.4, 0.9, and 1.1 s, respectively). Lowering the cutoff frequency progressively improved model fits (Figure 6C). Temporal shifts in input signals increased accordingly, with a model of 0.5 Hz cutoff (0.9 s delay) significantly improving peak response predictions for shrinking stimuli, compared with the point neuron model (p values 0.97, 0.98, 0.58, 10^{-6}, and 10^{-11} for cutoff frequencies 3.5, 2.5, 1.5, 0.5, and 0.35 Hz, Mann-Whitney U test; Figure 6C). The best performance was achieved at 0.35 Hz (1.1 s delay; Figures 6C and 6D). However, the temporal delays induced by this model are not physiologically plausible but instead resemble the time interval that the visual stimuli take to fully expand or shrink (0.95 s).

Second, we modeled the spatiotemporal activation of retinotopically distributed inputs by convolving the retinal inputs with a quadratic kernel (Figure 6B). This kernel simulates the sequential recruitment of inputs during stimulus expansion or shrinkage by approximating their temporal activation profile based on stimulus area, which scales quadratically with disk radius ($A \propto r^2$). This captures the aggregate effect of changing input strength over time but does not account for the precise position of each input along the dendritic arbor of a wide-field neuron. Despite its simplicity, this phenomenological model accurately reproduced wide-field neuron responses, performing significantly better to the point neuron model and comparable to the best low-pass filter model (p values 10^{-13} and 0.56, respectively; Figures 6C and 6D; see also Figure S6).

To assess the generalizability of our models, we tested them on a withheld dataset featuring expanding, shrinking, and dimming disks presented at three additional edge speeds (15°/s, 30°/s, 60°/s, and 120°/s, corresponding to movement durations of 1.9, 0.95, 0.48, and 0.24 s, respectively). The original dataset had an edge speed of 30°/s. On average, the slowest shrinking disk (15°/s) elicited the highest peak amplitudes (Figure 6E). These responses were best captured by the model incorporating the spatial arrangement of inputs and dendrites with peak amplitudes indistinguishable from measured responses (mean difference of peaks 0.02 ± 0.05 SD, $p = 0.14$, Wilcoxon signed-rank; Figure 6F). This model also provided the most accurate predictions for lower peak amplitudes in response to fast shrinking disks (120°/s), outperforming both the linear point neuron and low-pass filter models (mean difference of peaks 0.02 ± 0.03 SD, $p = 0.38$, Wilcoxon signed-rank; mean difference from point neuron and best low-pass filter model: −0.14 ± 0.06 and −0.13 ± 0.06 SD, p values 10^{-4} and 10^{-4}, Mann-Whitney U; Figure 6F).

The most effective way to capture wide-field neuron response properties is by accounting for the spatial arrangement of synaptic inputs along their dendrites. Applying a spatiotemporal activation kernel accurately reconstructs peak responses to behaviorally relevant visual stimuli, emphasizing the evolutionary advantage of wide-field neurons' extensive dendritic arbors.

To further refine our model, we incorporated depth-dependent filtering to account for layer-specific inputs along the dendritic tree (Figure 2H). Retinal inputs to the upper dendritic layers (depth < 150 μm) underwent spatiotemporal filtering, while inputs to the lower layers (>150 μm) remained unaltered (Figure 7A). This reduced model complexity to just 12 parameters while preserving predictive power, with peak amplitudes indistinguishable from measured responses for almost all speeds (mean peak differences −0.07 ± 0.10, −0.05 ± 0.07, 0.01 ± 0.06, and 0.12 ± 0.04, p values 0.48, 0.36, 0.99, and 10^{-5} for 15°/s, 30°/s, 60°/s, and 120°/s, Wilcoxon signed-rank; Figure 7B), outperforming the point neuron model despite fitting the same number of parameters (see also Figure S6). By restricting each input to a specific layer, this model minimizes wiring costs while maximizing coding efficiency, underscoring the evolutionary significance of retinotopically organized, layer-constrained inputs in integrating and encoding dynamic visual information.

DISCUSSION

Our findings demonstrate that dendritic morphology and the spatial organization of inputs are not merely a structural feature but serve as a computational substrate enabling selective filtering of salient motion cues. The layered arrangement of inputs along the dendritic tree of wide-field neurons supports structured processing of visual signals from distinct retinal ganglion cell types. This architecture permits simultaneous multiplexing of motion patterns characteristic of approaching, receding, and passing objects. By selectively amplifying slow-moving edges, wide-field neurons enhance detection of

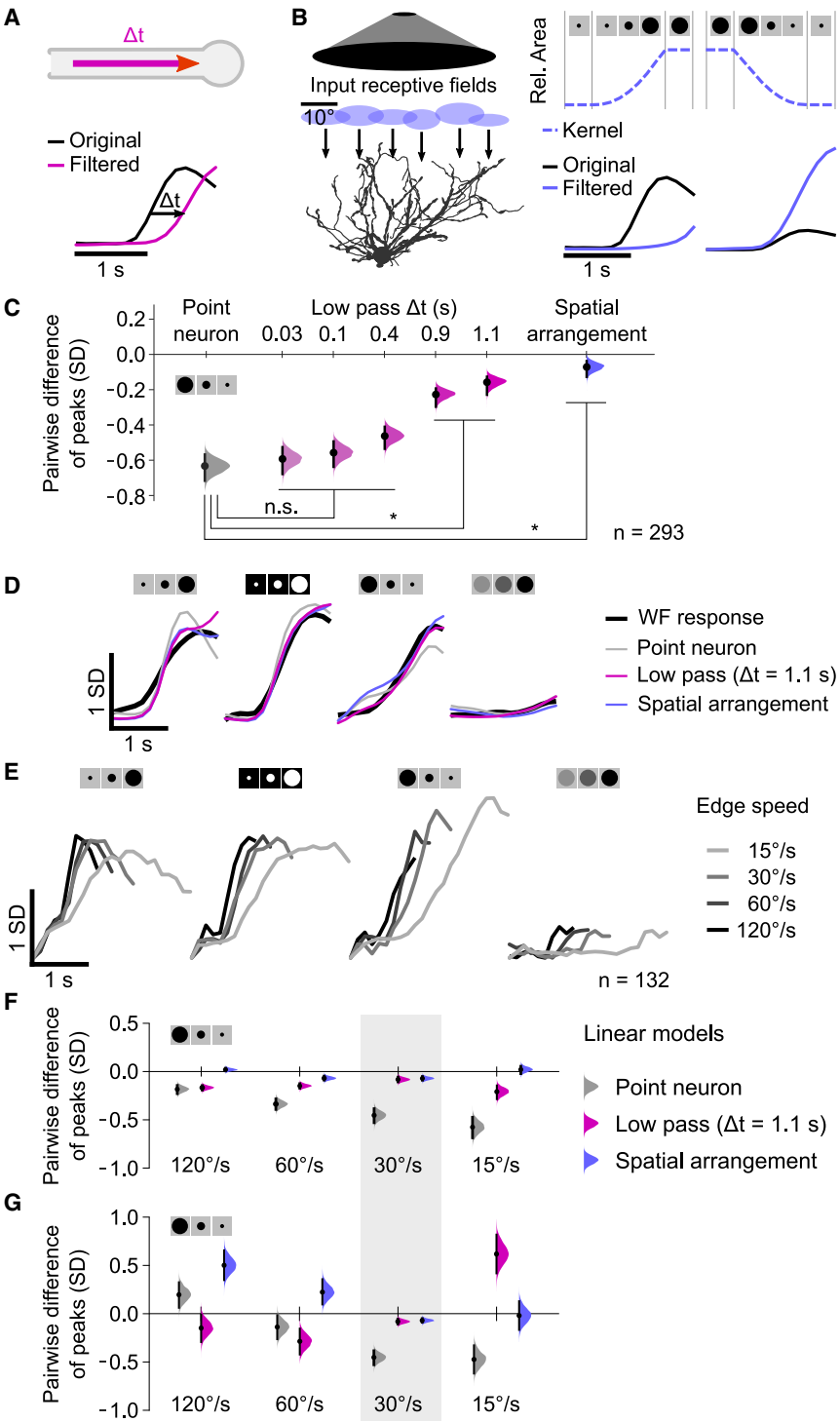

Figure 6. Accounting for low-pass filtering and spatiotemporal integration of inputs by dendrites improves model performance

(A) Low-pass filtering of retinal inputs induces signal delay. Original input: black; filtered input: pink.

(B) Left: spatial arrangement of inputs and dendrites. Right: spatiotemporal activation is modeled by a kernel. Original input: black; filtered input: purple.

(C) Pairwise differences between peak responses of wide-field neurons and model fits to the shrinking stimulus. Point neuron: gray; low-pass filtering: pink; spatially arranged dendrites: purple. Dots and error bars indicate the mean and 95% confidence interval of the resampled distribution. *P* values in comparison with the point neuron model: 0.97, 0.98, 0.58, 10^{-6}, and 10^{-11} for cutoff frequencies 3.5, 2.5, 1.5, 0.5, and 0.35 Hz of the low-pass model and 10^{-13} for the spatial arrangement model, Mann-Whitney U test.

(D) Mean responses of wide-field neurons (black) and a subset of the linear fits shown in (C). Data as in Figure 1.

(E) Mean wide-field neuron responses to expanding, shrinking, and dimming disks at four different edge speeds (15°/s, 30°/s, 60°/s, and 120°/s, grayscale-coded).

(F) Pairwise differences of peaks between wide-field neuron responses and model fits to different speeds. Dots and error bars indicate the mean and 95% confidence interval of the resampled distribution.

(G) Pairwise differences of peaks as in (F), but with a model fitted to the original speed of 30°/s. Dots and error bars indicate the mean and 95% confidence interval of the resampled distribution.

See also Figure S6.

potential threats and opportunities, a computation critical for ethologically relevant decisions.

This capacity for selective filtering is not a simple reflection of retinal inputs but arises from *de novo* computations performed by wide-field neurons. While retinal ganglion cells predominantly encode expanding stimuli, wide-field neurons exhibit balanced tuning to both expanding and shrinking stimuli. This transformation arises from the structured integration of the diverse set of retinal inputs, rather than from local inhibition, extracting motion features not explicitly present in retinal signals. Inputs arrive in a depth-specific manner, with each ganglion cell type targeting a distinct layer of the colliculus. The estimated input depths align with those of identified ganglion cell types, such as Foxp2+ and Smi32+ populations.[2,46–48] This layered organization has functional consequences. For example, transient alpha retinal ganglion cells in the deeper layers (150–250 μm) likely convey looming signals, while small transient retinal ganglion cells in the superficial layers (50–150 μm) integrate over a large field of view, aiding detection of small moving objects. Sustained Off alpha retinal ganglion cells, in the intermediate layers (100–150 μm), may contribute to integrating movement of large objects. The interaction between sustained Off alpha and small transient retinal ganglion cells likely underpins strong

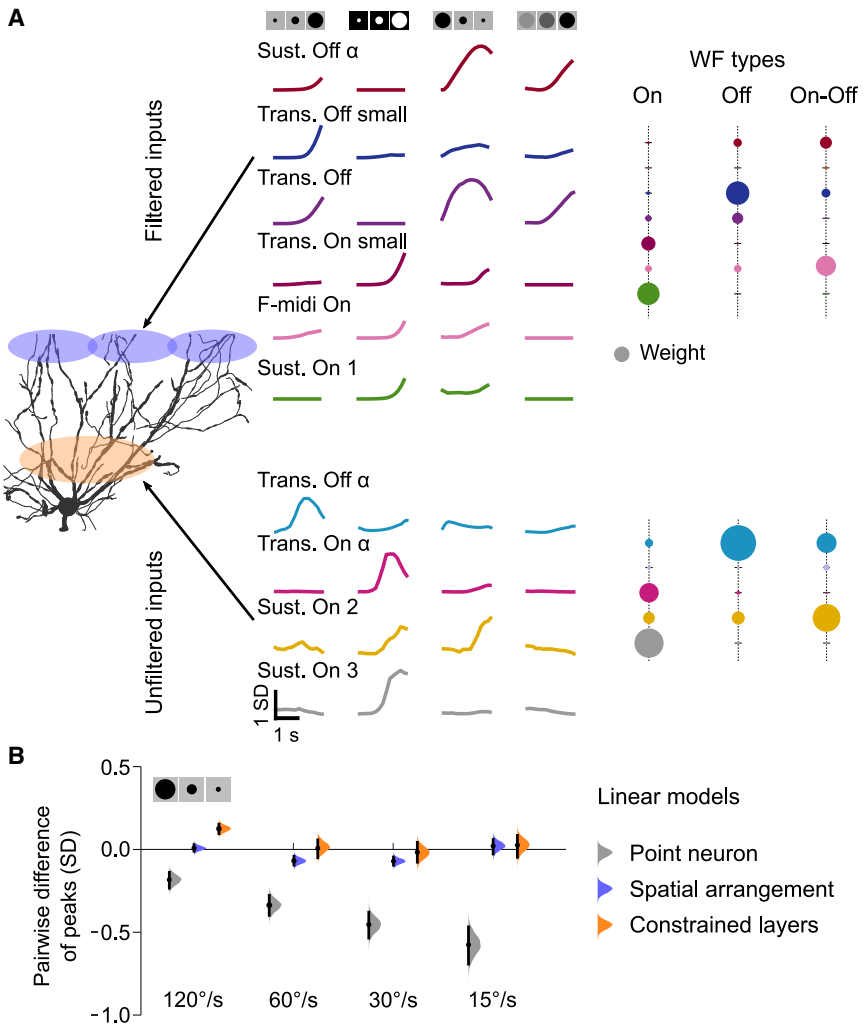

Figure 7. A model with layer-specific spatiotemporal integration captures wide-field neuron responses

(A) Model incorporating layer-specific spatiotemporal integration: retinal inputs to upper layers (depth < 150 μm; see Figure 2H) are filtered by a spatiotemporal kernel, while inputs to lower layers (depth > 150 μm) remain unaltered. Left: filtered inputs. Right: weights of filtered inputs.

(B) Pairwise differences between peak wide-field neuron responses and model fits, comparing models with spatially arranged inputs with and without constrained layers. Black dots with error bars represent mean and 95% confidence intervals from bootstrapping.

See also Figure S6.

responses to receding stimuli, where proximal inputs may facilitate propagation of signals from distal dendrites.

Our modeling demonstrates that the layer-specific organization of inputs is sufficient to account for wide-field neuron responses with minimal complexity. Assigning each ganglion cell type a layer-specific spatial filter reduces the need for additional mechanisms. This principle parallels findings from artificial neural networks, where architectures based on local connectivity achieve greater efficiency and generalization than fully connected models.[49,50] In biological systems, such anatomical efficiency is likely important given the constraints imposed by limited space and metabolic resources.[51] By leveraging spatially organized input patterns, wide-field neurons extract motion cues critical for innate behaviors, illustrating how anatomical structure directly supports computational efficiency and efficacy in neural circuits.

Our best-performing model relies on linear integration and the spatial organization of dendrites and inputs. Although large neurons often exhibit low-pass filtering (for example, dopamine and teleost neurons with time constants of ~100 ms[52,53]), the fitted delays in our model (~1 s) likely reflect stimulus duration rather than intrinsic properties. Wide-field neurons possess active dendritic properties,[39] yet nonlinear integration did not significantly improve model performance. Instead, as noted by Gale and Murphy,[39] small stimulations of distal dendrites can reliably trigger somatic spikes, supporting linear summation, where fast I_h currents[54] may aid summation and contribute to rebound effects in distal dendrites.

This study used calcium imaging, which imposes two limitations: low temporal resolution and limited bandwidth. These constraints restricted our analysis to the estimated firing rates of recorded neurons. Nonetheless, calcium imaging was appropriate, as inputs and outputs were measured separately without inferring spike timing. To assess potential brightness saturation, we compared patch-clamp and calcium signals in retinal ganglion cells. Wide-field neurons showed low baseline activity (~0 Hz) and moderate firing rates in response to motion (up to 50 Hz),[25,39] keeping signals within the indicator's linear range. However, local sodium-driven dendritic events were likely missed. Wide-field neurons also receive modulatory inputs from other brain areas, which likely adjust output according to internal state and context.

Our findings illustrate how structured dendritic architecture enables efficient extraction of salient motion cues critical for innate behaviors. The selective amplification of slow motion by wide-field neurons supports ethologically relevant decisions, such as whether to freeze or flee, revealing how spatial organization of inputs enhances computational efficiency. Future work combining cell-type-specific manipulations with behavioral assays and biophysical modeling will clarify how wide-field neurons contribute to visually guided actions. As a model system, wide-field neurons provide a cellular framework for linking dendritic computation to natural behavior and for investigating sensory salience and its dysregulation in neurodevelopmental and anxiety-related disorders.

RESOURCE AVAILABILITY

Lead contact

Further information and requests for resources and reagents should be directed to and will be fulfilled by the lead contact, Karl Farrow (karl.farrow@kuleuven.be).

Materials availability

This study did not generate new unique reagents.

Data and code availability

- Preprocessed data have been deposited at Zenodo and are publicly available as of the date of publication at https://doi.org/10.5281/zenodo.15640801.
- All original code has been deposited at Zenodo and is publicly available at https://doi.org/10.5281/zenodo.15640801 as of the date of publication.
- Any additional information required to reanalyze the data reported in this paper is available from the lead contact upon request.

ACKNOWLEDGMENTS

We thank Bram Nuttin and Pedro Gonçalves (NERF, Leuven, Belgium) for discussions on the modeling aspects and Xu Han (VIB-CBD, Leuven, Belgium) who implemented the band-pass noise stimulus. Initial rabies aliquots (Rabies-CVS-deltaG-GCaMP6f and Rabies-CVS-deltaG-Chr2-YFP) as well as cell lines for virus amplification (Neuro2a-G and Neuro2a-EnvA) were provided by Andy Murray (Sainsbury Wellcome Center, London, UK). This work was supported by the FWO, Belgium (G094616N to K.F., G091719N to K.F., 1205421N to N.K.K., and 12S7917N/12S7920N to K.R.) and the European Union's Horizon 2020 research and innovation program under the Marie Sklodowska-Curie grant agreement no. 796102 to N.K.K. and no. 665501 to K.R.

AUTHOR CONTRIBUTIONS

Conceptualization, N.K.K., V.B., and K.F.; experimental setup and development, N.K.K., C.L., J.Z., K.R., and K.F.; *in vivo* imaging, N.K.K.; retinal imaging, C.L.; sparse labeling, J.Z.; analysis, N.K.K., C.L., V.B., and K.F.; computational models, N.K.K. and N.B.; software, N.K.K. and K.R.; and writing and editing, N.K.K., V.B., and K.F.

DECLARATION OF INTERESTS

The authors declare no competing interests.

DECLARATION OF GENERATIVE AI AND AI-ASSISTED TECHNOLOGIES IN THE WRITING PROCESS

During the preparation of this work, the authors used ChatGPT to check for consistency and correct sentence structure. After using this tool, the authors reviewed and edited the content as needed and take full responsibility for the content of the publication.

STAR★METHODS

Detailed methods are provided in the online version of this paper and include the following:

SUPPLEMENTAL INFORMATION

Supplemental information can be found online at https://doi.org/10.1016/j.cub.2025.06.060.

Received: March 5, 2025
Revised: May 27, 2025
Accepted: June 23, 2025
Published: July 15, 2025

REFERENCES

1. Lafourcade, M., Van Der Goes, M.-S.H., Vardalaki, D., Brown, N.J., Voigts, J., Yun, D.H., Kim, M.E., Ku, T., and Harnett, M.T. (2022). Differential dendritic integration of long-range inputs in association cortex via subcellular changes in synaptic AMPA-to-NMDA receptor ratio. Neuron *110*, 1532–1546.e4. https://doi.org/10.1016/j.neuron.2022.01.025.
2. Martersteck, E.M., Hirokawa, K.E., Evarts, M., Bernard, A., Duan, X., Li, Y., Ng, L., Oh, S.W., Ouellette, B., Royall, J.J., et al. (2017). Diverse Central Projection Patterns of Retinal Ganglion Cells. Cell Rep. *18*, 2058–2072. https://doi.org/10.1016/j.celrep.2017.01.075.
3. Douglas, R.J., Martin, K.A.C., and Whitteridge, D. (1989). A Canonical Microcircuit for Neocortex. Neural Comput. *1*, 480–488. https://doi.org/10.1162/neco.1989.1.4.480.
4. Xu, N.L., Harnett, M.T., Williams, S.R., Huber, D., O'Connor, D.H., Svoboda, K., and Magee, J.C. (2012). Nonlinear dendritic integration of sensory and motor input during an active sensing task. Nature *492*, 247–251. https://doi.org/10.1038/nature11601.
5. Sedigh-Sarvestani, M., and Fitzpatrick, D. (2022). What and Where: Location-Dependent Feature Sensitivity as a Canonical Organizing Principle of the Visual System. Front. Neural Circuits *16*, 834876. https://doi.org/10.3389/fncir.2022.834876.
6. Molotkov, D., Ferrarese, L., Boissonnet, T., and Asari, H. (2023). Topographic axonal projection at single-cell precision supports local retinotopy in the mouse superior colliculus. Nat. Commun. *14*, 7418. https://doi.org/10.1038/s41467-023-43218-x.

7. Dräger, U.C., and Hubel, D.H. (1976). Topography of visual and somatosensory projections to mouse superior colliculus. J. Neurophysiol. *39*, 91–101. https://doi.org/10.1152/jn.1976.39.1.91.

8. Kerr, J.N.D., de Kock, C.P.J., Greenberg, D.S., Bruno, R.M., Sakmann, B., and Helmchen, F. (2007). Spatial Organization of Neuronal Population Responses in Layer 2/3 of Rat Barrel Cortex. J. Neurosci. *27*, 13316–13328. https://doi.org/10.1523/JNEUROSCI.2210-07.2007.

9. Rall, W., Burke, R.E., Smith, T.G., Nelson, P.G., and Frank, K. (1967). Dendritic location of synapses and possible mechanisms for the monosynaptic EPSP in motoneurons. J. Neurophysiol. *30*, 1169–1193. https://doi.org/10.1152/jn.1967.30.5.1169.

10. Branco, T., Clark, B.A., and Häusser, M. (2010). Dendritic Discrimination of Temporal Input Sequences in Cortical Neurons. Science *329*, 1671–1675. https://doi.org/10.1126/science.1189664.

11. Stuart, G.J., and Sakmann, B. (1994). Active propagation of somatic action potentials into neocortical pyramidal cell dendrites. Nature *367*, 69–72. https://doi.org/10.1038/367069a0.

12. Sakmann, B., and Neher, E. (1983). Single-Channel Recording (Springer).

13. Poirazi, P., Brannon, T., and Mel, B.W. (2003). Arithmetic of subthreshold synaptic summation in a model CA1 pyramidal cell. Neuron *37*, 977–987. https://doi.org/10.1016/S0896-6273(03)00148-X.

14. Gidon, A., Zolnik, T.A., Fidzinski, P., Bolduan, F., Papoutsi, A., Poirazi, P., Holtkamp, M., Vida, I., and Larkum, M.E. (2020). Dendritic action potentials and computation in human layer 2/3 cortical neurons. Science *367*, 83–87. https://doi.org/10.1126/science.aax6239.

15. Ran, Y., Huang, Z., Baden, T., Schubert, T., Baayen, H., Berens, P., Franke, K., and Euler, T. (2020). Type-specific dendritic integration in mouse retinal ganglion cells. Nat. Commun. *11*, 2101. https://doi.org/10.1038/s41467-020-15867-9.

16. Chander, P.R., Hanson, L., Chundekkad, P., and Awatramani, G.B. (2024). Neural Circuits Underlying Multifeature Extraction in the Retina. J. Neurosci. *44*, e0910232023. https://doi.org/10.1523/JNEUROSCI.0910-23.2023.

17. Acarón Ledesma, H., Ding, J., Oosterboer, S., Huang, X., Chen, Q., Wang, S., Lin, M.Z., and Wei, W. (2024). Dendritic mGluR2 and perisomatic Kv3 signaling regulate dendritic computation of mouse starburst amacrine cells. Nat. Commun. *15*, 1819. https://doi.org/10.1038/s41467-024-46234-7.

18. Román Rosón, M.R., Bauer, Y., Kotkat, A.H., Berens, P., Euler, T., and Busse, L. (2019). Mouse dLGN Receives Functional Input from a Diverse Population of Retinal Ganglion Cells with Limited Convergence. Neuron *102*, 462–476.e8. https://doi.org/10.1016/j.neuron.2019.01.040.

19. Rompani, S.B., Müllner, F.E., Wanner, A., Zhang, C., Roth, C.N., Yonehara, K., and Roska, B. (2017). Different modes of visual integration in the lateral geniculate nucleus revealed by single-cell-initiated transsynaptic tracing. Neuron *93*, 767–776.e6. https://doi.org/10.1016/j.neuron.2017.01.028.

20. Liang, L., Fratzl, A., Goldey, G., Ramesh, R.N., Sugden, A.U., Morgan, J.L., Chen, C., and Andermann, M.L. (2018). A Fine-Scale Functional Logic to Convergence from Retina to Thalamus. Cell *173*, 1343–1355.e24. https://doi.org/10.1016/j.cell.2018.04.041.

21. Basso, M.A., and May, P.J. (2017). Circuits for Action and Cognition: A View from the Superior Colliculus. Annu. Rev. Vision Sci. *3*, 197–226. https://doi.org/10.1146/annurev-vision-102016-061234.

22. Davidson, R.M., and Bender, D.B. (1991). Selectivity for relative motion in the monkey superior colliculus. J. Neurophysiol. *65*, 1115–1133. https://doi.org/10.1152/jn.1991.65.5.1115.

23. Lu, X., Hu, Z., Xin, Y., Yang, T., Wang, Y., Zhang, P., Liu, N., and Jiang, Y. (2024). Detecting biological motion signals in human and monkey superior colliculus: a subcortical-cortical pathway for biological motion perception. Nat. Commun. *15*, 9606. https://doi.org/10.1038/s41467-024-53968-x.

24. Shang, C., Chen, Z., Liu, A., Li, Y., Zhang, J., Qu, B., Yan, F., Zhang, Y., Liu, W., Liu, Z., et al. (2018). Divergent midbrain circuits orchestrate escape and freezing responses to looming stimuli in mice. Nat. Commun. *9*, 1232. https://doi.org/10.1038/s41467-018-03580-7.

25. Hoy, J.L., Bishop, H.I., and Niell, C.M. (2019). Defined Cell Types in Superior Colliculus Make Distinct Contributions to Prey Capture Behavior in the Mouse. Curr. Biol. *29*, 4130–4138.e5. https://doi.org/10.1016/j.cub.2019.10.017.

26. Baden, T., Berens, P., Franke, K., Román Rosón, M., Bethge, M., and Euler, T. (2016). The functional diversity of retinal ganglion cells in the mouse. Nature *529*, 345–350. https://doi.org/10.1038/nature16468.

27. Goetz, J., Jessen, Z.F., Jacobi, A., Mani, A., Cooler, S., Greer, D., Kadri, S., Segal, J., Shekhar, K., Sanes, J.R., et al. (2022). Unified classification of mouse retinal ganglion cells using function, morphology, and gene expression. Cell Rep. *40*, 111040. https://doi.org/10.1016/j.celrep.2022.111040.

28. Sümbül, U., Song, S., McCulloch, K., Becker, M., Lin, B., Sanes, J.R., Masland, R.H., and Seung, H.S. (2014). A genetic and computational approach to structurally classify neuronal types. Nat. Commun. *5*, 3512. https://doi.org/10.1038/ncomms4512.

29. Sans-Dublanc, A., Chrzanowska, A., Reinhard, K., Lemmon, D., Nuttin, B., Lambert, T., Montaldo, G., Urban, A., and Farrow, K. (2021). Optogenetic fUSI for brain-wide mapping of neural activity mediating collicular-dependent behaviors. Neuron *109*, 1888–1905.e10. https://doi.org/10.1016/j.neuron.2021.04.008.

30. Isa, K., Sooksawate, T., Kobayashi, K., Kobayashi, K., Redgrave, P., and Isa, T. (2020). Dissecting the tectal output channels for orienting and defense responses. eNeuro *7*, ENEURO.0271-20.2020. https://doi.org/10.1523/ENEURO.0271-20.2020.

31. De Malmazet, D., Kühn, N.K., Li, C., and Farrow, K. (2024). Retinal origin of orientation but not direction selective maps in the superior colliculus. Curr. Biol. *34*, 1222–1233.e7. https://doi.org/10.1016/j.cub.2024.02.001.

32. May, P.J. (2006). The mammalian superior colliculus: Laminar structure and connections. Prog. Brain Res. *151*, 321–378. https://doi.org/10.1016/S0079-6123(05)51011-2.

33. Hong, Y.K., Kim, I.J., and Sanes, J.R. (2011). Stereotyped axonal arbors of retinal ganglion cell subsets in the mouse superior colliculus. J. Comp. Neurol. *519*, 1691–1711. https://doi.org/10.1002/cne.22595.

34. Kay, J.N., De La Huerta, I., Kim, I.-J., Zhang, Y., Yamagata, M., Chu, M.W., Meister, M., and Sanes, J.R. (2011). Retinal Ganglion Cells with Distinct Directional Preferences Differ in Molecular Identity, Structure, and Central Projections. J. Neurosci. *31*, 7753–7762. https://doi.org/10.1523/JNEUROSCI.0907-11.2011.

35. Ahmadlou, M., and Heimel, J.A. (2015). Preference for concentric orientations in the mouse superior colliculus. Nat. Commun. *6*, 6773. https://doi.org/10.1038/ncomms7773.

36. Li, Y.T., Turan, Z., and Meister, M. (2020). Functional Architecture of Motion Direction in the Mouse Superior Colliculus. Curr. Biol. *30*, 3304–3315.e4. https://doi.org/10.1016/j.cub.2020.06.023.

37. Gupta, D., Młynarski, W., Sumser, A., Symonova, O., Svatoň, J., and Joesch, M. (2023). Panoramic visual statistics shape retina-wide organization of receptive fields. Nat. Neurosci. *26*, 606–614. https://doi.org/10.1038/s41593-023-01280-0.

38. Liang, Y., Lu, R., Borges, K., and Ji, N. (2023). Stimulus edges induce orientation tuning in superior colliculus. Nat. Commun. *14*, 4756. https://doi.org/10.1038/s41467-023-40444-1.

39. Gale, S.D., and Murphy, G.J. (2016). Active dendritic properties and local inhibitory input enable selectivity for object motion in mouse superior colliculus neurons. J. Neurosci. *36*, 9111–9123. https://doi.org/10.1523/JNEUROSCI.0645-16.2016.

40. Gale, S.D., and Murphy, G.J. (2014). Distinct representation and distribution of visual information by specific cell types in mouse superficial superior colliculus. J. Neurosci. *34*, 13458–13471. https://doi.org/10.1523/JNEUROSCI.2768-14.2014.

41. Reinhard, K., Li, C., Do, Q., Burke, E.G., Heynderickx, S., and Farrow, K. (2019). A projection specific logic to sampling visual inputs in mouse superior colliculus. eLife *8*, e50697. https://doi.org/10.7554/eLife.50697.

42. Wei, P., Liu, N., Zhang, Z., Liu, X., Tang, Y., He, X., Wu, B., Zhou, Z., Liu, Y., Li, J., et al. (2015). Processing of visually evoked innate fear by a non-canonical thalamic pathway. Nat. Commun. *6*, 6756. https://doi.org/10.1038/ncomms7756.

43. Zingg, B., Chou, X.L., Zhang, Z.G., Mesik, L., Liang, F., Tao, H.W., and Zhang, L.I. (2017). AAV-Mediated Anterograde Transsynaptic Tagging: Mapping Corticocollicular Input-Defined Neural Pathways for Defense Behaviors. Neuron *93*, 33–47. https://doi.org/10.1016/j.neuron.2016.11.045.

44. Shang, C., Liu, Z., Chen, Z., Shi, Y., Wang, Q., Liu, S., Li, D., and Cao, P. (2015). A parvalbumin-positive excitatory visual pathway to trigger fear responses in mice. Science *348*, 1472–1477. https://doi.org/10.1126/science.aaa8694.

45. Münch, T.A., da Silveira, R.A., Siegert, S., Viney, T.J., Awatramani, G.B., and Roska, B. (2009). Approach sensitivity in the retina processed by a multifunctional neural circuit. Nat. Neurosci. *12*, 1308–1316. https://doi.org/10.1038/nn.2389.

46. Kim, I.-J., Zhang, Y., Meister, M., and Sanes, J.R. (2010). Laminar restriction of retinal ganglion cell dendrites and axons: Subtype-specific developmental patterns revealed with transgenic markers. J. Neurosci. *30*, 1452–1462. https://doi.org/10.1523/JNEUROSCI.4779-09.2010.

47. Huberman, A.D., Manu, M., Koch, S.M., Susman, M.W., Lutz, A.B., Ullian, E.M., Baccus, S.A., and Barres, B.A. (2008). Architecture and Activity-Mediated Refinement of Axonal Projections from a Mosaic of Genetically Identified Retinal Ganglion Cells. Neuron *59*, 425–438. https://doi.org/10.1016/j.neuron.2008.07.018.

48. Rousso, D.L., Qiao, M., Kagan, R.D., Yamagata, M., Palmiter, R.D., and Sanes, J.R. (2016). Two Pairs of ON and OFF Retinal Ganglion Cells Are Defined by Intersectional Patterns of Transcription Factor Expression. Cell Rep. *15*, 1930–1944. https://doi.org/10.1016/j.celrep.2016.04.069.

49. Chavlis, S., and Poirazi, P. (2025). Dendrites endow artificial neural networks with accurate, robust and parameter-efficient learning. Nat. Commun. *16*, 943. https://doi.org/10.1038/s41467-025-56297-9.

50. Lindsey, J., Ocko, S.A., Ganguli, S., and Deny, S. (2019). A Unified Theory of Early Visual Representations from Retina to Cortex through Anatomically Constrained Deep CNNs. Preprint at bioRxiv. https://doi.org/10.1101/511535.

51. Sterling, P., and Laughlin, S. (2015). Principles of Neural Design (The MIT Press). https://doi.org/10.7551/mitpress/9780262028707.001.0001.

52. Blumhagen, F., Zhu, P., Shum, J., Schärer, Y.P.Z., Yaksi, E., Deisseroth, K., and Friedrich, R.W. (2011). Neuronal filtering of multiplexed odour representations. Nature *479*, 493–498. https://doi.org/10.1038/nature10633.

53. Tsutsui, H., and Oka, Y. (2002). Slow removal of Na+ channel inactivation underlies the temporal filtering property in the teleost thalamic neurons. J. Physiol. *539*, 743–753. https://doi.org/10.1113/jphysiol.2001.013061.

54. Endo, T., Tarusawa, E., Notomi, T., Kaneda, K., Hirabayashi, M., Shigemoto, R., and Isa, T. (2008). Dendritic Ih ensures high-fidelity dendritic spike responses of motion-sensitive neurons in rat superior colliculus. J. Neurophysiol. *99*, 2066–2076. https://doi.org/10.1152/jn.00556.2007.

55. Schindelin, J., Arganda-Carreras, I., Frise, E., Kaynig, V., Longair, M., Pietzsch, T., Preibisch, S., Rueden, C., Saalfeld, S., Schmid, B., et al. (2012). Fiji: An open-source platform for biological-image analysis. Nat. Methods *9*, 676–682. https://doi.org/10.1038/nmeth.2019.

56. Peng, H., Bria, A., Zhou, Z., Iannello, G., and Long, F. (2014). Extensible visualization and analysis for multidimensional images using Vaa3D. Nat. Protoc. *9*, 193–208. https://doi.org/10.1038/nprot.2014.011.

57. Coupé, P., Munz, M., Manjón, J.V., Ruthazer, E.S., and Collins, D.L. (2012). A CANDLE for a deeper in-vivo insight. Med. Image Anal. *16*, 849–864. https://doi.org/10.1016/j.media.2012.01.002.

58. de Malmazet, D., Kühn, N.K., and Farrow, K. (2018). Retinotopic Separation of Nasal and Temporal Motion Selectivity in the Mouse Superior Colliculus. Curr. Biol. *28*, 2961–2969.e4. https://doi.org/10.1016/j.cub.2018.07.001.

59. Lee, D.D., and Seung, H.S. (1999). Learning the parts of objects by non-negative matrix factorization. Nature *401*, 788–791. https://doi.org/10.1038/44565.

STAR★METHODS

KEY RESOURCES TABLE

REAGENT or RESOURCE	SOURCE	IDENTIFIER
Antibodies		
Chicken, polyclonal, anti-GFP (1:500)	Thermo Fisher Scientific	Cat# A-10262; RRID: AB_2534023
Donkey, Alexa 488, anti-chicken (1:500)	Immuno-Jackson	Cat# 703-545-155; RRID: AB_2340375
Goat, polyclonal, anti-ChAT (1:200)	Millipore	Cat# AB144P; RRID: AB_11214092
Dondey, Alexa 633, anti-goat (1:500)	Thermo Fisher Scientific	Cat# A-21082; RRID: AB_10562400
Mouse, monoclonal, anti-SMI32 (1:1000)	Biolend	Cat# 801701; RRID: AB_2564642
Dondey, Cy3, anti-mouse (1:400)	Immuno-Jackson	Cat# 715-165-151; RRID: AB_2315777
Donkey, Dylight 405, anti-mouse (1:500)	Thermo Fisher Scientific	Cat# A-48257; RRID: AB_2884884
Donkey, Dylight 405, anti-mouse (1:500)	ImmunoJackson	Cat# 715-475-150; RRID: AB_2340839
Rabbit, polyclonal, anti-CART (1:500)	Phoenix Pharmaceuticals	H-003-62; RRID: AB_2313614
Donkey, DyLight 405, anti-rabbit (1:400)	Immuno-Jackson	Cat# 715-475-150; RRID: AB_2340839
Donkey, Alexa 555, anti-rabbit (1:500)	Thermo Fisher Scientific	Cat# A-31570; RRID: AB 2313501
Goat, polyclonal, anti-FOXP2 (1:500)	abcam	Cat# 1307; RRID: AB_1268914
Donkey, Alexa 555, anti-goat (1:300)	abcam	Cat# ab150130; RRID:AB_2927775
Rabbit, polyclonal, anti-RFP (1:1000)	Rockland	Cat# 600-401-379; RRID: AB_2209751
DAPI (1:200)	Roche	Cat# 10276236001
Bacterial and virus strains		
AAV1-hSyn-Flex-GCaMP6s	Addgene	Cat# 100845-AAV1; RRID: Addgene_100845
EnvA-RVΔG-GCaMP6f: EnvA-coated rabies CVS-N2c-ΔG-GCaMP6f	This paper based on aliquots obtained from Laboratory of Andy Murray	N/A
HSV-Flex-TVA-G-mCherry: HSV-hEF1α-LS1L-TVA950-T2A-n2c(G)-IRES-mCherry	R. Neve (MGH)	RN716
HSV-Flex-mCherry: HSV-hEF1α-LS1L-IRES-mCherry	R. Neve (MGH)	RN413
BHK cells	Laboratory of Botond Roska/ Laboratory of Karl-Klaus Conzelmann	N/A
B7GG cells	Laboratory of Botond Roska/ Laboratory of Karl-Klaus Conzelmann	N/A
BHK-EnvA cells	Laboratory of Botond Roska/ Laboratory of Karl-Klaus Conzelmann	N/A
HEK293T-TVA cells	Laboratory of Botond Roska/ Laboratory of Karl-Klaus Conzelmann	N/A
Chemicals, peptides, and recombinant proteins		
Lipophilic tracers DiI, DiD, DiO	Thermo Fisher Scientific	Cat# D7776, D7757, D275
10x PBS	VWR	Cat# 437117K
1x PBS	VWR	Cat# 444057Y
Histofix 4%	Roche	Cat# P087.5
Normal Donkey Serum	Millipore	Cat# 30-100ML
10% Bovine Albumin	Sigma	Cat# SRE0036-250ML
DMEM, high glucose	Thermo Fisher Scientific	Cat# 41965062
Trypsin 0.05%	Thermo Fisher Scientific	Cat# 25300054
Fetal Bovine Serum (FBS)	Thermo Fisher Scientific	Cat# 10270106
2,2'-thiodiethanol (TDE)	Sigma	Cat# 166782-500G
ProLong® Gold Antifade Mounting Medium	Thermo Fisher Scientific	Cat# P36934
Sodium Azide (NaN3)	Sigma	Cat# S2002-100G

(*Continued on next page*)

Continued

REAGENT or RESOURCE	SOURCE	IDENTIFIER
Triton X-100	Sigma	Cat# S8875
Sodium Chloride (NaCl)	Sigma	Cat# S7653-250G
Potassium Chloride (KCl)	Sigma	Cat# P5405-25G
Calcium Chloride (CaCl2)	Sigma	Cat# C5670-100G
Magnesium Chloride (MgCl2)	Sigma	Cat# 4880
D-glucose (Dextrose)	Sigma	Cat# D9434-250G
Sodium phosphate monobasic (NaH2PO4)	Sigma	Cat# S5011
Sodium Hydroxide (NaOH)	Sigma	Cat# 655104-500G
Sodium bicarbonate (NaHCO3)	Sigma	Cat# S8875-1KG
Deposited data		
Preprocessed raw data	This paper	Zenodo: https://doi.org/10.5281/zenodo.15640801
Experimental models: Organisms/strains		
Mus musculus Ntsr1-GN209-Cre: STOCK Tg(Ntsr1-Cre) GN209Gsat/Mmucd	Laboratory of Keisuke Yonehara	Genset: 030780-UCD
Mus musculus Gad2-IRES-Cre: STOCK Gad2tm2(cre)Zjh/J	The Jackson Laboratory	Cat# 010802; RRID: IMSR_JAX:010802
Software and algorithms		
Code to analyze the preprocessed raw data	This paper	Zenodo: https://doi.org/10.5281/zenodo.15640801
Neural models	This paper	Zenodo: https://doi.org/10.5281/zenodo.15640801
Fiji	Schindelin et al.[55]	RRID: SCR_002285
MATLAB	Mathworks	RRID: SCR_001622
Zen lite	Zeiss	N/A
ChAT band detector	Reinhard et al.[41]	https://github.com/farrowlab/ChATbandsDetection
PYTHON 3.9	Python Software Foundation	RRID: SCR_008394
CaImAn 1.7.1	Flatiron Institute	RRID: SCR_021533
Vaa3D	Peng et al.[56]	https://home.penglab.com/proj/vaa3d
CANDLE	Coupé et al.[57]	N/A
GNU Octave	Free Software Foundation	RRID: SCR_01439
Psychophysics Toolbox	Psychtoolbox	RRID: SCR_002881
WaveSurfer (version: 0.918)	Janelia Research Campus	RRID: SCR_021529
ScanImage	Vidrio Technoloies	http://scanimage.vidriotechnologies.com
Other		
Rapid Flow Filters 0.2 μm pore size	VWR	Cat# 514-0027
Wiretrol® II capillary micropipettes	Drumond Scientific	Cat# 5-000-2005
Borosilicate glass	Sutter Instrument	Cat# BF100-20-10
Glass capillaries, Ø 3 mm, custom fine saw cut to L=1.5 mm	Hilgenberg	1915017
Round borosilicate cover glasses, Ø 3 mm, 0.1 mm thickness	Multichannel systems	640720
UV-curing optical adhesive	Norland	61
Metabond dental cement	Crown & Bridge	N/A
Super-Bond C&B kit for self-curing adhesive resin cement	Sun Medical	N/A
Laser-Based Micropipette Puller	Sutter Instrument	Cat# P-2000
Small Animal Stereotaxic Workstation	Narishige	Cat# SR-5N
Stereotaxic Micromanipulator	Narishige	Cat# SM-15R
Hydraulic Oil Micromanipulator	Narishige	Cat# MO-10
Oil Microinjector	Narishige	Cat# IM-9B
Two-photon microscope	Scientifica	Serial# 14200

(*Continued on next page*)

Continued

REAGENT or RESOURCE	SOURCE	IDENTIFIER
780 nm LED light source	Thorlabs	Cat# M780L3
Patch-Clamp amplifier	Molecular Device	Axon Multiclamp 700B
Patch-Clamp microscope	Scientifica	Slice Scope
Patch-Clamp manipulator	Scientifica	Serial# 301311
Zeiss LSM 710 confocal microscope	Zeiss	Cat# LSM710
Mai Tai HP Ti:Sapphire laser	Spectra Physics	N/A
B-Scope 2p microscope	Thorlabs	N/A

EXPERIMENTAL MODEL AND STUDY PARTICIPANT DETAILS

Mice

All experimental procedures were approved by the Ethical Committee for Animal Experimentation (ECD) of the KU Leuven and followed the European Communities Guidelines on the Care and Use of Laboratory Animals (014-2018/EEC, 166–2018/EEC). Both male and female adult transgenic mice (1–3 months old) were used in our experiments. To target wide-field neurons and their retinal inputs, *Ntsr1-GN209-Cre* mice were used (10 female, 5 male and 10 female, 5 male, respectively). Inhibitory neurons of the colliculus were targeted using *Gad2-IRES-Cre* mice (4 female, 4 male). Mice were heterozygously bread with C57Bl6J mice and kept on a 12-h light-dark cycle (lights on at 7:00), and sterilized food pellets and water were provided *ad libitum*.

METHOD DETAILS

Labeling of wide-field neurons and Gad2 neurons of the colliculus for two-photon imaging

To label wide-field neurons and Gad2 neurons of the superior colliculus for in vivo two-photon calcium imaging, a floxed viral vector expressing the fluorescent calcium indicator GCaMP6s (AAV1-hSyn-Flex-GCaMP6s, titer 2.956 x 10^{13} GC/mL, Addgene) is injected into the superior colliculus of *Ntsr1-GN209-Cre* and *Gad2-IRES-Cre* mice, respectively, and a cranial head plate and cannula window is implanted above the frontal two thirds of the superior colliculus, following a procedure previously developed in the lab.[58]

Anesthesia is induced at the beginning with isoflurane 3% in 0.8 l/min O_2 in a closed chamber and then kept with a combination of ketamine (75mg/kg) and medetomidine (1mg/kg). During the whole procedure animals are kept at physiological temperature by a homeothermic blanket. After deep anesthesia is achieved, eye ointment is applied to protect the eyes from drying out. Before starting any surgical procedure, the paw of the animal is pinched to check for the absence of pedal reflex (indicator of a proper anesthesia). The scalp is shaved and depilated (depilatory cream), disinfected (70% EtOH and betadine®), 0.5% lidocaine is applied locally and the skin opened/removed; the periosteum is removed, and the lateral and posterior muscles are retracted. Vetbond TM is applied to open skin and exposed muscle. A head plate is attached to the skull using cyanoacrylate glue and Metabond®; a 3.5 mm craniotomy is performed; the brain is washed with sterile aCSF; a small cortex trunk (3 mm in diameter, 1 mm deep) is gently aspired under visual guidance until the surface of the SC is exposed. A cannula window (3 mm diameter, 3 mm height) is wedged into the craniotomy. Animals recover in separate cages and are treated with analgesic and antibiotics for 72 hours (Vetergesic, Ceva Animal Health Ltd; Emdotrim, ecuphar, BE-V235523) and monitored for 4 days.

Labeling of retinal ganglion cells innervating wide-field neurons

Retinal ganglion cells that project to wide-field neurons were labeled with a transsynaptic viral tracing strategy, combining a floxed helper virus (HSV-hEF1α-LS1L-TVA950-T2A-n2c(G)-IRES-mCherry) with an EnvA-coated CVS-N2c-ΔG-GCaMP6f rabies virus in *Ntsr1-GN209-Cre* mice.[41] Animals were quickly anesthetized with Isoflurane (Iso-vet 1000mg/ml) and then injected with a mixture of Ketamine and Medetomidine (0.75 mL Ketamine (100 mg/mL) + 1 mL Medetomidine (1 mg/mL) + 8.2 mL Saline). Mice were placed in a stereotaxic workstation (Narishige, SR-5N). Dura tear (NOVARTIS, 288/28062-7) was applied to protect the eyes.

First, the helper virus was injected into the lateral posterior nucleus of the thalamus using micropipettes (Wiretrol® II capillary micropipettes, Drumond Scientific, 5-000-2005) with an open tip of around 30 μm and an oil-based hydraulic micromanipulator MO-10 (Narishige) for stereotactic injections. The injection coordinates for a 4 weeks old mouse with a bregma-lambda distance of 4.7 mm were AP: -1.85; ML: ±1.50; DV: 2.50 mm. As the mice were different in body size, we adjusted the coordinates for each mouse according to their bregma-lambda distance. To label the injection sites, DiD (Thermo, D7757) was used to coat the pipette tip. We injected in total 100-400 nl helper virus in single doses of up to 200 nl with a waiting time of 5-10 min after each injection.

Following the injections, the wound was closed using Vetbond tissue adhesive (3M,1469). After surgery, mice were allowed to recover on top of a heating pad and were provided with soft food and water containing antibiotics (emdotrim, ecuphar, BE-V235523).

Twenty-one days later, we injected the rabies virus into the superior colliculus using the same method as for the helper virus injections. As the retinotopic location of the first injection into the lateral pulvinar is uncertain, we covered as much as possible of the superficial layer of the superior colliculus during the second injection to maximize the labeling of cells in the retina. We injected

100-200 nl of rabies virus at a depth of 1.7 – 1.8 mm at the corners of a 1 mm^2 square anterior of lambda and starting at the midline.

Sparse labeling of wide-field neurons

We sparsely labeled wide-field neurons by injecting a diluted HSV-hEF1α-LS1L-mCherry (1:128) into the lateral posterior nucleus of the thalamus of *Ntsr1-GN209-Cre* mice (see Labeling of retinal ganglion cells).

In vivo colliculus recordings

Before recordings started, animals were acclimated to the experimenter for a week. Mice were handled for 10 min a day for a period of three days. Mice were head fixed on an air-cushioned Styrofoam ball for progressive periods of time through five days, starting from 10 min to an hour.

The superior colliculus was scanned with a SpectraPhysics MaiTai femtosecond laser at 920 nm through a Thorlabs B-Scope microscope equipped with a resonance scanner and a Nikon 16x objective with 3 mm focal length. The laser power was adjusted and blanked during fly back of the galvo mirror by a Pockels cell. For imaging the somas of wide-field neurons, the nominal power at the end of the objective is kept at 90 mW while an area of 250 x 250 μm^2 is imaged with a resolution of 512 x 512 pxls. This results in an imaging rate of 30 Hz. For imaging the dendrites of wide-field neurons, the superior colliculus is scanned across 5 planes with a piezo element starting at the surface and going down to 250 μm. The laser power is adjusted by depth following an exponential, starting at 30 mW and saturating at 120 mW. Fluorescence of the sample is filtered by a Thorlabs GFP emission filter (MF525-39) and photons captured by a Hamamatsu PMT.

The B-Scope is operated and imaging frames are recorded using ScanImage 11 (Vidrio Technologies). Imaging frames and visual stimuli are synchronized by yoking ScanImage to WaveSurfer 0.913 (HHMI Janelia Research Campus), which lets us capture imaging frame and visual stimulus triggers and the spinning speed of the Styrofoam ball. Further, square pulse triggers of 60 Hz are sent to a face camera (Mako G-030B, Allied Vision Technologies), recording the ipsilateral side of the mouse's face. The camera frames are recorded with custom-written software by Joao Couto (bitbucket.org/jpcouto/labcams) in Python 2.7.

During calcium imaging, visual stimuli were displayed on a 78 x 40 cm^2 LCD screen at 30 cm distance from the mouse and centered at 0° elevation and 20° azimuth of the contralateral eye. Visual stimuli were generated using a custom-written software in GNU Octave (Eaton et al. 2019) with Psychtoolbox-3.

Ex vivo retina recordings

Visual responses of labeled retinal ganglion cells were recorded with two-photon calcium imaging (n = 1471 cells, 14 mice) or whole-cell loose patch recordings (n = 112 cells, 11 mice). Calcium responses were confirmed with simultaneous whole-cell patch recordings (n = 5 cells, 2 mice, Figure S2).

For *ex vivo* recordings of retinal ganglion cells, retinas were isolated from mice that were dark-adapted for a minimum of 30 minutes. Retina isolation was done under deep red illumination in Ringer's medium (110 mM NaCl, 2.5 mM KCl, 1 mM CaCl2, 1.6 mM MgCl2, 10 mM D-glucose, 22 mM NaHCO3, bubbled with 5% CO2/95% O2, pH 7.4). The retinas were then mounted ganglion cell-side up on filter paper (Millipore, HAWP01300) that had a 3.5 mm wide rectangular aperture in the center, and superfused with Ringer's medium at 32–36°C in the microscope chamber for the duration of the experiment.

Electrophysiological recordings were made using an Axon Multiclamp 700B amplifier (Molecular Devices) and borosilicate glass electrodes (BF100-50-10, Sutter Instrument). Signals were digitized at 20 kHz (National Instruments) and acquired using WaveSurfer software (version: 0.918) written in MATLAB. The spiking responses were recorded using the patch clamp technique in loose cell-attached mode with electrodes pulled to 3-5 MΩ resistance and filled with Ringer's medium. To visualize the pipette, Alexa 555 was added to the Ringer's medium.

Fluorescent cells were targeted for recording using a two-photon microscope (Scientifica) equipped with a Mai Tai HP two-photon laser (Spectra Physics) integrated into the electrophysiological setup. To facilitate targeting, two-photon fluorescent images were overlaid with the IR image acquired through a CCD camera. Infrared light was produced using the light from an LED. For some cells, z-stacks were acquired using ScanImage (Vidrio Technologies).

Retinas are visually stimulated with a LED projector whose light is passed through a lens system and dimmed by a neutral density filter at the end of the optical pathway. The retina is oriented in a way that the nasal direction is facing down with respect to the projected image. During two-photon imaging, the stimulus is presented in blue to avoid overstimulating the PMTs.

Stimuli were generated with an LCD projector (Samsung, SP F10M) at a refresh rate of 60 Hz, controlled with custom software written in Octave based on Psychtoolbox. The projector produced a light spectrum that ranged from ∼430 nm to ∼670 nm. The power produced by the projector was 240 mW/cm2 at the retina. A combination of a neutral density filter and a short pass filter (cutoff wavelength = 475 nm) were used to control the stimulus intensity in logarithmic steps. Recordings were performed with filters decreasing the stimulus intensity by 1-2 log units.

Visual stimuli

The following visual stimuli were presented to the explanted retina and the behaving mice (white, gray and black correspond to 100%, 0% and -100% Weber contrast). A TTL pulse was sent at the beginning and the end of each repeat for later alignment.

Full-field stimulus

A fixed sequence of full-field contrast modulation was presented across the full screen (90° x 50°). The sequence starts with 2 s black, 3 s white, 3 s black and 2 s gray screen and is followed by two sinusoidal temporal contrast modulations, interleaved by 2 s of gray screen. The first sinusoidal is of 100% contrast and increases linearly in frequency from 0 to 8 Hz within 8 s. The second sinusoidal is of 2 Hz frequency and linearly increases in amplitude from 0 to 100% within 8 s. The second sinusoidal is followed by 2 s gray and 2 s black screen.[18,26] The whole sequence is repeated 10 times.

Expanding disk

A black or white disk linearly expanded from 2° to 50° within 0.95 s at the center of a gray or black screen, respectively. The stimulus was repeated 10 times, interleaved by 3 s of gray or black screen, respectively.

Shrinking disk

A black disk linearly shrunk from 50° to 2° of diameter within 0.95 s at the center of a gray screen. The stimulus was repeated 10 times, interleaved by 3 s of gray screen.

Dimming disk

A disk of 50° diameter linearly dimmed from background gray to black within 0.95 s at the center of the screen. The stimulus was repeated 10 times, interleaved by 3 s of gray screen.

Sweeping disk

A black or white disk of different diameter (2°, 8° and 32°) moved with 30°/s and 160°/s in two directions (left to right, right to left) across the center of a gray or black screen, respectively. Each combination of direction, size and speed was repeated 3 times in random order and interleaved by 3 s of gray or black screen, respectively.

Bandpass noise (in vivo only)

A patch of 50° was shown for 2 s on gray background with band-pass-filtered spatiotemporal white-noise patterns of different temporal (0.5, 1, 2, 4, 8 Hz) and spatial cut-off frequencies (0.02, 0.04, 0.08, 0.16, 0.32 cycles/°). Each pattern was randomly generated, and each condition repeated 4 times in random order, interleaved by 3 s of gray screen.

Retina immunohistochemistry

After *ex vivo* recordings, retinas were fixed in 4% paraformaldehyde (Histofix, ROTH, P087.5mm) with 100 mM sucrose for 30 min at 4°C, and then transferred to a 24-well plate filled with 1x PBS and washed 3 times for 10 min at room temperature or transferred into 15 ml 1x PBS and washed overnight or longer at 4 °C. After washing, retinas were transferred to wells containing 10% sucrose in 1x PBS with 0.1% NaN3 (w/v) and allowed to sink for a minimum of 30 min at room temperature. Then retinas were transferred to wells containing 20% sucrose in 1x PBS with 0.1% NaN3 (w/v) and allowed to sink for a minimum of 1 hour at room temperature. Finally, retinas were put into 30% sucrose in 1x PBS with 0.1% NaN3 (w/v) and allowed to sink overnight at 4°C. The next day, freeze-cracking was performed: retinas were frozen on a slide fully covered with 30% sucrose for 3-5 min on dry ice. The slides were then thawed at room temperature. The freeze-thaw cycle was repeated two times. Retinas were washed 3 times for 10 min each in 1x PBS, followed by incubation with blocking buffer (10% NDS, 1% BSA, 0.5% TritonX-100, 0.02% NaN3 in 1x PBS) for at least 1 hour at room temperature or overnight at 4°C with gentle shaking.

Primary antibody goat against FOXP2 (abcam1307, 1:2000) was added after blocking and retinas were incubated for 5 days under constant gentle shaking at 4°C. They were prepared in 5% NDS, 0.3% TritonX-100 in 1x PBS. After incubation, retinas were washed 3 times for 15 min in 1x PBS with 0.3% TritonX-100 before being transferred into the secondary antibody solution (Alexa555 donkey anti-goat abcam150130, 1:300); prepared in 1xPBS overnight at 4°C. The second day, retinas were washed 3 times in 1x PBS and incubated in the second primary antibody solution for 5 days under constant gentle shaking at room temperature. The second primary antibodies were rabbit anti-GFP (Invitrogen, A-11122, 1:500), goat anti-ChAT (Chemicon, Ab144P, 1:200) and mouse SMI32 (Biolend, 801701,1:1000). They were prepared in 3% NDS, 1% BSA, 0.5% TritonX-100, 0.02% NaN3 in 1x PBS. Retinas were then washed 3 times for 10 min in 1x PBS with 0.5% TritonX-100. After washing, the retinas were incubated in the secondary antibody solution overnight at 4°C. Secondary antibodies were Alexa488 donkey anti-chicken (ImmunoJackson, 703-545-155, 1:500), Alexa 633 donkey anti-goat (Invitrogen A-21082, 1:500) and DyLight 405 donkey anti-mouse (Thermo, A-48257 or ImmunoJackson, 715-475-150, 1:300); prepared in 3% NDS, 1% BSA, 0.5% TritonX-100, 0.02% NaN3 in 1x PBS). Retinas were then washed 3 times in 1x PBS with 0.5% TritonX-100 and 1 time in 1x PBS.

For mounting, we used 2,2′-Thiodiethanol (TDE) (Sigma, 166782-500G) (Staudt et al., 2007) to exchange the water in the sample. To achieve this, retinas were incubated in different concentration of TDE buffer (10% -> 25% -> 50% -> 97%) for at least 30 minutes each. Then the retinas were embedded in ProLong® Gold Antifade Mountant (Thermo, P36934) and gently covered with a #0 coverslip (MARIENFEL, 0100032, No.0, 18*18 mm). To avoid squeezing the retinas, we put 4 strips of Parafilm (Parafilm, PM999) around the retina before adding the coverslip. Some of the retinas were mounted in 97% TDE with DABCO (Sigma, 290734) after immersion into TDE. Some retinas were mounted with ProLong® Gold Antifade Mountant directly after washing. Afterward, nail polish was used to prevent evaporation and the samples were stored in darkness at 4°C.

Brain immunohistochemistry

Extracted brains were post-fixed in 4% PFA overnight at 4°C. Vibratome coronal sections (100 mm) were collected in 1x PBS and were incubated in blocking buffer (1x PBS, 0.3% Triton X-100, 10% Donkey serum) at room temperature for at least 1 hour or overnight. Then brain slices were incubated with primary antibodies solution for 2-3 days at 4°C with shaking. Slices were later washed

3 times for 10 min each in 1x PBS with 0.3% TritonX-100 and incubated in secondary antibody solution for 2-3 days at 4°C. Primary and secondary antibody were chicken anti-GFP (1:1000) and Alexa488 donkey anti-chicken (1:800), respectively, for GCaMP6s labeled cells and rabbit anti-RFP (1:1000) and Alexa555 donkey anti-rabbit (1:500) for sparsely labeled cells. Nuclei were stained with DAPI (1:1000) together with the secondary antibody solution. Sections were then again washed 3 times for 10 min in 1x PBS with 0.3% TritonX-100 and 1 time in 1x PBS, covered with mounting medium and a glass coverslip. PBS were prepared with 0.02% NaN3.

Confocal microscopy

Confocal microscopy was performed on a Zeiss LSM 710 microscope. Overview images of the retina and brain were obtained with a 10x (plan-APOCHROMAT 0.45 NA, Zeiss) objective. The following settings were used: zoom 1.2, 5x5-tiles with 15% overlap, 2.37 μm/pixel resolution. For single retina ganglion cells and sparsely labeled wide-field neurons, we used a 63x (plan-APOCHROMAT 1.4 NA, Zeiss) objective. The following settings were used: zoom 0.7, 2x2-tiles or more (depending on size and number of cells) with 15% overlap. This resulted in an XY-resolution of 0.38 μm/pixel and a Z-resolution between 0.3 μm/pixel. The Z-stacks covered approximately 50 μm in depth.

QUANTIFICATION AND STATISTICAL ANALYSIS

Data processing and analysis was performed in Python and MATLAB.

Two-photon image registration and ROI extraction

Two-photon imaging frames were registered, and ROIs determined using NNMF with CaImAn 1.7.1 (Flatiron Institute) in Python 3.4. The signal decay time for the model was adjusted to GCaMP6s (1.4 s). ΔF/F values of these selected ROIs were used for further analysis. ROIs of collicular wide-field neurons, Gad2 neurons and retinal ganglion cells were obtained separately from ROIs representing dendritic compartments of collicular wide-field neurons.

Clustering of ROI responses

Calcium responses were baseline-subtracted by the minimum and normalized by the standard deviation across all stimuli. K-Means clustering was performed on the correlation matrix of concatenated responses. For wide-field neurons, responses to expanding, shrinking, and dimming stimuli were used. Dendritic compartments were clustered based on full-field responses, while Gad2 neurons and retinal ganglion cells were clustered using responses to full-field, expanding, shrinking, and dimming stimuli.

To determine the number of clusters, we took the average of the best cluster number obtained from Silhouette, Calinski-Harabasz and Davies-Bouldin score.

Cell selection

The repeats of visual stimuli and neural responses were aligned by using the simultaneously recorded stimulus start and imaging frame triggers. For each presented stimulus, a quality index of each ROI was calculated. The quality index was calculated from the variance of ΔF/F across time, $\mathrm{var}(\cdot)_t$, and the mean across stimulus repeats, $\mathrm{E}(\cdot)_r$, as follows: $\mathrm{QI} = \mathrm{var}(\mathrm{E}(\Delta F/F)_r)_t / \mathrm{E}(\mathrm{var}(\Delta F/F)_t)_r$. Cells were included into the analysis if they were visually responsive with a quality index above 0.3 for at least one of the recorded stimuli.

Identification of retinal ganglion cell types

We identified the recorded retinal ganglion cells in the stained retinas by template matching (FIJI[55] plugin), allowing us to link visual responses to molecular types. For a subset (n = 122 cells, 12 retinas), the dendritic arbors were traced, allowing for morphological classification. Using the *On*- and *Off* ChAT bands, formed by the starburst amacrine cells, as landmarks of retinal organization, we calculated the stratification density profile of every traced retinal ganglion cell and measured the soma size. Retinal ganglion cells were then identified based on molecular labeling, soma size and stratification profile by matching them manually to existing databases.[26–28,41]

Morphology of retinal ganglion cells

To annotate dendritic trees in confocal Z-stacks, we used Ariadne-Service GmbH (Switzerland) for automated tracing. Prior, the confocal Z-stacks of retinal ganglion cells were denoised (CANDLE package,[57] MATLAB) and down-sampled (XYZ = 0.5 x 0.5 x 0.35 μm per pixel). ChAT band positions were extracted using a convolutional neural network (V-Net) trained to detect and segment these structures (https://github.com/farrowlab/ChATbandsDetection).[41] The ChAT band locations were then used to warp the dendritic tree, aligning it in 3D space.[28]

Dendritic tree depth profiles were computed by normalizing Z-positions and applying a low-pass Fourier filter. The dendritic area was estimated via convex hull approximation, with diameters calculated as D = 2*(area / π)1/2. The soma area was measured manually using the convex hull tool in ImageJ.

Comparison of imaged and patched retinal ganglion cell signals

To infer how linear the relationship between inferred calcium signals from patch clamp experiments and measured calcium signals from imaging experiments, we calculated the area under the curve (AUC) of the peak-normalized averaged responses of imaged and patched cells of each type. An AUC value of 0.5 corresponds to a perfect linear relationship, whereas values above and below 0.5 indicate a supralinear and sublinear behavior of the measured calcium signal: Sustained Off alpha 0.54, F-mini Off 0.46, Transient Off Small 0.40, Transient Off Alpha 0.39, Transient Off 0.35, F-mini On 0.60, Transient On small 0.51, Transient On Alpha 0.47, F-midi On 0.55, Sustained On 1 0.41, Sustained On 2 0.50, Sustained On 3 0.41.

Morphology of sparsely labeled wide-field neurons

A sparsely labeled wide-field neuron was traced and stitched across four coronal slices in Vaa3D.[56] The extracted start and end points of dendritic segments and their thickness were used to plot a coronal projection of the neuron.

Depth distribution of dendritic clusters and retinal ganglion cell inputs

we determined the number of ROIs per scanning plane and corrected for sampling bias by weighting them relative to the total ROIs in each plane, yielding a depth distribution of dendritic ROIs per cluster.

To estimate the stratification depth of each retinal ganglion cell type, we identified the wide-field neuron dendritic ROI with the strongest correlation coefficient (>0.4) for each retinal ganglion cell. The depths of these identified dendritic ROIs were then used to calculate a depth distribution for each retinal ganglion cell type using the method above.

Sparsity index

To test the amount of convergence and divergence of retinal inputs onto different dendritic clusters, we calculated the Gini index G for each row and column of the weight matrix, respectively. The distributions were compared to a uniform distribution across clusters and cell types.

Difference of peaks

We calculated the difference of peaks between wide-field neuron responses and their fitted counterparts for each stimulus by subtracting the maximum value of the normalized, baseline-subtracted response from the maximum of the corresponding fit.

Expansion selectivity index

An expansion selectivity index was calculated for each recorded wide-field neuron and retinal ganglion cell based on peak responses to black expanding disks r_e and white expanding, black shrinking and dimming disks r_s using the formula $I = (r_e - r_s)/(r_e + r_s)$. Distributions were then visualized using kernel density estimation, with a smoothing bandwidth determined by Scott's rule.

Noise correlation analysis of wide-field neuron dendrites and cell bodies

To assess whether distinct dendritic response types coexist within individual wide-field neurons, we performed noise correlation analysis between dendritic compartments and somata. We used responses to black expanding disks, a stimulus that reliably evoked calcium transients in both compartments. For each stimulus repetition, we subtracted the trial-averaged response from individual traces to isolate noise fluctuations, and computed pairwise Pearson correlations across all dendrite–soma pairs in each recording. Each dendritic compartment was then assigned to the soma with the highest correlation coefficient. A connection was considered reliable if the noise correlation exceeded 0.7. Using this criterion, approximately one third of dendritic compartments could be confidently assigned to a soma. Many of these somata were associated with multiple dendritic compartments exhibiting different response dynamics, spanning between two and six of the nine defined functional clusters. This suggests that individual WF neurons integrate diverse retinal inputs via functionally distinct dendritic domains.

Computational models

Models were implemented in Julia 1.7.

Non-negative linear regression

A non-negative linear regression model[59] was fitted using the NNLS package in Julia. The nonnegative constraint is in line with the excitatory nature of the retinal inputs to the colliculus and ensures sparsity.

Nonnegative linear regression was used in four different models, 1) a point neuron model integrating inputs from retinal ganglion cell types, 2) a point neuron model integrating inputs from retinal ganglion cells types and inhibitory interneurons, 3) a model considering low pass filtering of the inputs and 4) a model considering the spatiotemporal integration of distributed inputs.

To fit the responses of wide-field neuron cell bodies to expanding, shrinking and dimming disks, we concatenated the responses to the presented stimuli and normalized the concatenated responses by their standard deviation.

Multilayer Perceptron

A multilayer perceptron was fitted using the Flux package in Julia. This model assumes a local summation of the excitatory retinal and inhibitory collicular inputs and nonlinear processing along the dendrites. A sigmoidal nonlinearity is used to capture supra- and

sublinear processing of the summed inputs along the dendrites. To implement the neural spiking threshold, a rectifying nonlinearity is used at the output node.

Models were fitted by gradient descent using the ADAM optimizer. An L1 penalty on the sum of all fitted parameters was introduced to ensure sparsity. Linear weights and biases were initialized with uniformly distributed random values between 0 and 1.

Models incorporating low pass filtering of inputs through dendrites

The non-negative linear regression model (see above) was fitted to an extended set of filtered retinal inputs, doubling the number of fitting parameters. A 4th-order Butterworth low-pass filter (cutoff: 0.4, 0.5, 1, 2, 3 Hz) generated additional inputs from the original inputs, and non-negative weights were fitted to the combined set of original and filtered inputs for each cutoff frequency.

Models incorporating the spatial organization of inputs and dendrites

To capture the spatial arrangement of inputs and dendrites, a spatiotemporal activation kernel was convolved with retinal responses to expanding and shrinking disks. This kernel accounted for the relative number of activated retinal inputs per 0.13 s time bin based on changes in disk surface area, producing a quadratically increasing or decreasing activation profile. The non-negative linear regression model (see above) was then fitted to the combined set of original and convolution-filtered retinal inputs.

To account for the layer-specific arrival of inputs onto the dendrites, we refined our model using depth-dependent filtering. For each retinal ganglion cell type, we estimated the arrival depth of its signals by correlating each cell's response with the dendritic signals across depth (see above), and averaging the resulting depth profile. Inputs whose average location was in the upper dendritic layers (<150 μm) were passed through a spatiotemporal filter, while those targeting deeper layers (>150 μm) remained unfiltered.

Extrapolation of retinal ganglion cell responses to different stimulus speeds

Responses to expanding, shrinking and dimming disks of different speeds were only recorded in wide-field neurons. Responses of retinal ganglion cells to slower and faster speeds were estimated by linear up and down sampling of the responses to the original stimulus, respectively.

Current Biology, Volume *35*

Supplemental Information

Dendritic architecture enables *de novo* computation of salient motion in the superior colliculus

Norma K. Kühn, Chen Li, Natalia Baimacheva, Janne Zimmer, Katja Reinhard, Vincent Bonin, and Karl Farrow

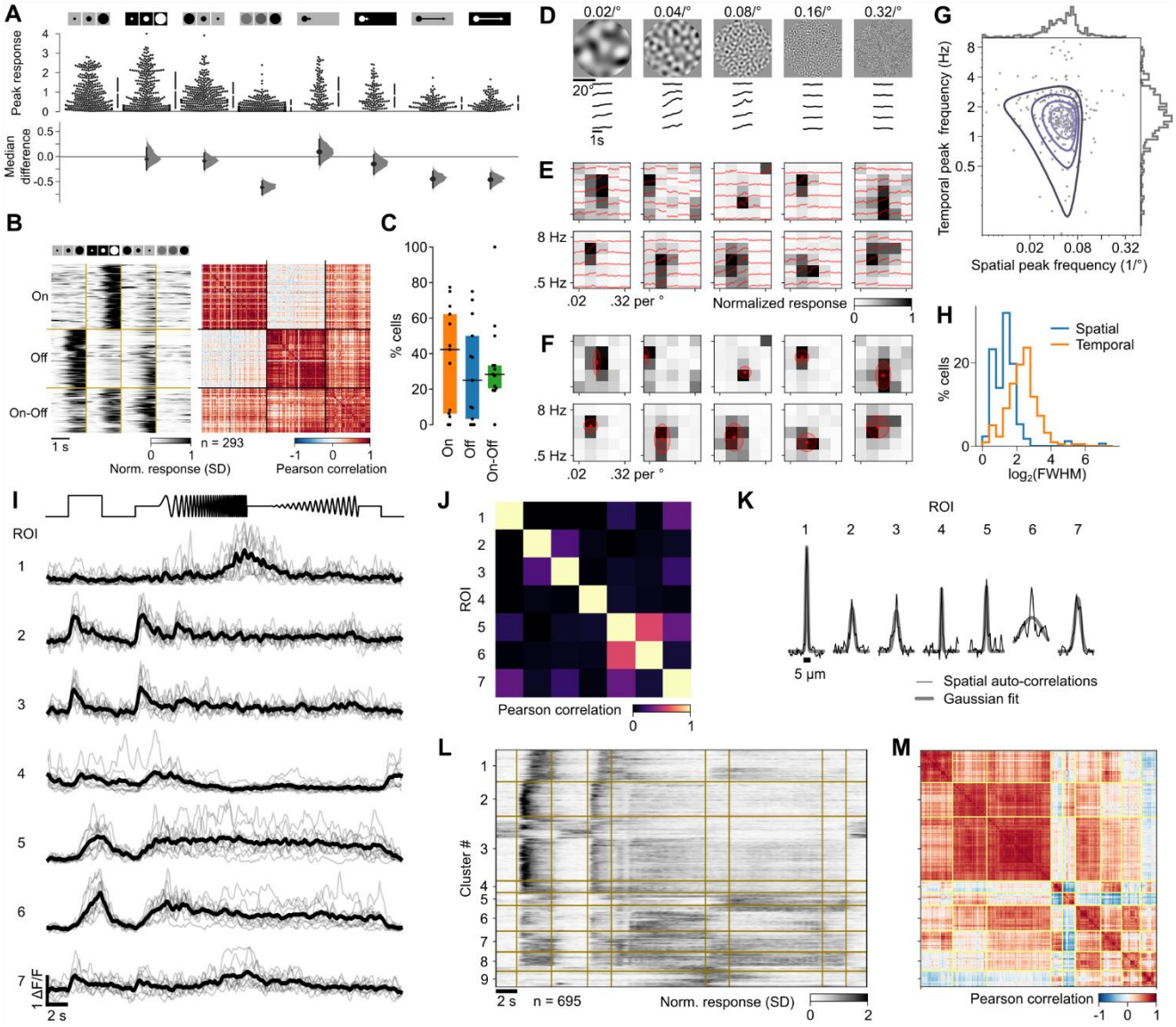

Figure S1. Additional Response Properties of Wide-Field Neurons and Noise Correlations in Dendrites, Related to Figure 1.

(A) Comparison of peak responses to expanding, shrinking and dimming disks and slow and fast 2° sweeping disks.

(B) Left: Heatmap normalized and clustered wide-field cell body responses. Right: Correlation matrix of response clusters.

(C) Proportion of On, Off, and On-Off wide-field cell bodies per recorded field of view. Vertical bars and boxes indicate median and interquartile range (IQR).

(D) Responses of an example wide-field neurons to two second snippets of spatiotemporal bandpass noise of different spatial (left to right) and temporal frequencies (top to bottom).

(E) Spatiotemporal frequency tuning curves of ten example wide-field cell bodies, with heatmap indicating normalized peak responses.

(F) 2D Gaussian fits to the tuning curves of example cell bodies. Red dots indicate the mean, and shaded circles represent the 1-σ range.

(G-H) Distributions of the spatiotemporal peak frequencies (D) and tuning widths (E) of the 2D Gaussian fits.

(I) Example responses of dendritic ROIs to the full-field stimulus across four different imaging planes from a single recording. Gray and black lines indicate individual and averaged trials from 10 stimulus repetitions.

(J) Temporal correlations of raw ROI responses in (A) across all trials.

(K) Spatial auto-correlations of ROIs across the widest dimension.

(L-M) Heatmap of normalized and clustered average responses (L) and correlation matrix (M). Data as in Figure 1.

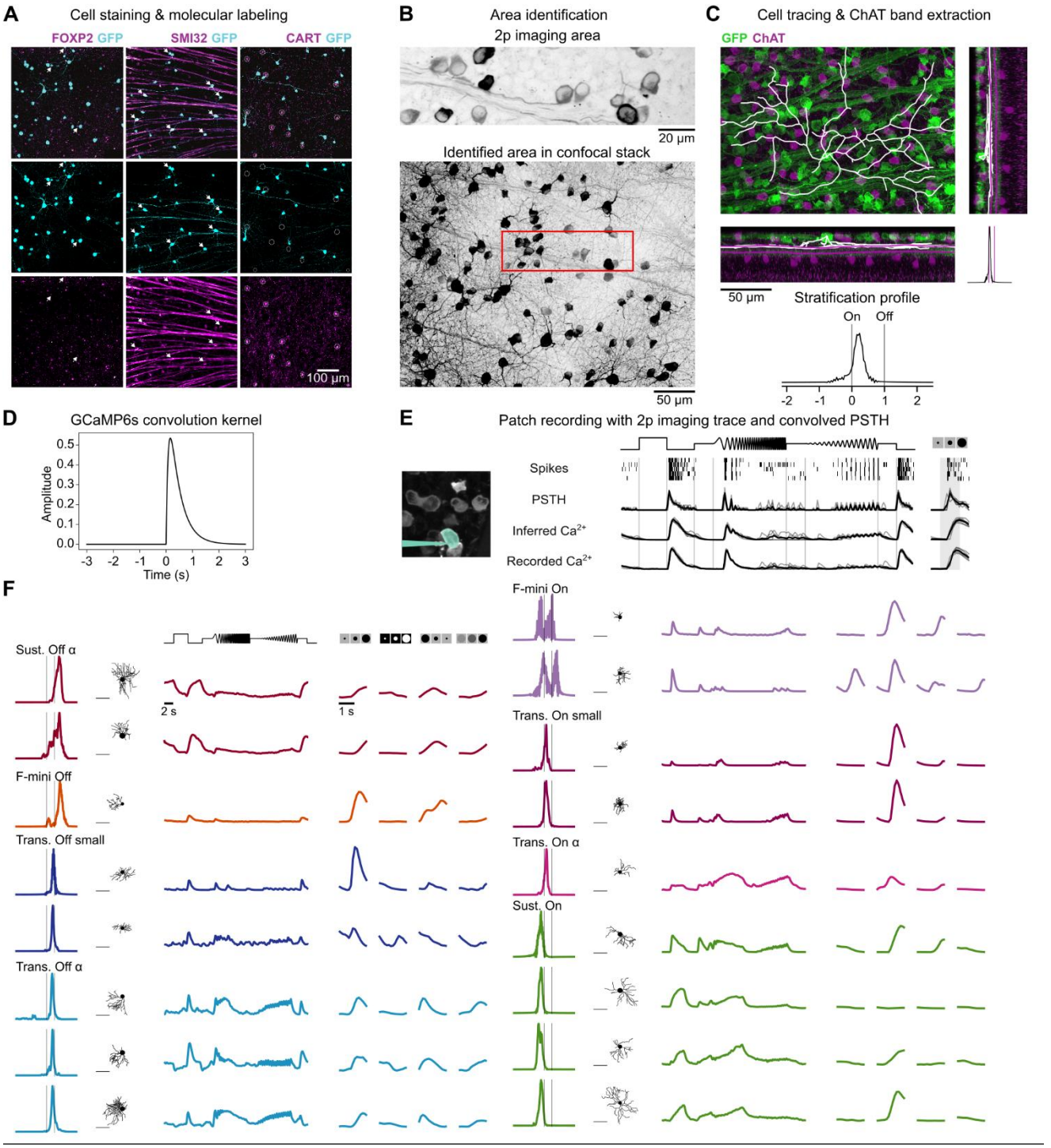

Figure S2. Identification of Retinal Ganglion Cells Projecting to Wide-Field Neurons, Related to Figure 2.

(A) Immunohistochemical labeling of retinal ganglion cells. GFP-labeled cells (cyan) co-stained for FOXP2, SMI32, or CART (magenta) to identify molecular subtypes.

(B) Post hoc identification of the two-photon imaging area (top) within a stained whole-mount retina (bottom). Both images are maximum projections of z-stacks, with the imaging area (red box) determined via template matching.

(C) High-resolution confocal imaging of recorded cells (0.3765 × 0.3765 × 0.3 µm³/pxl). Top: dendrite tracing of GFP-labeled cells (green). Bottom: extracted stratification profile relative to ON- and OFF-ChAT bands, with traced dendrites (white) and detected ChAT bands (purple).

(D) GCaMP6s convolution kernel used to convolve spike responses.

(E) Comparison of patch-clamp PSTHs with two-photon calcium signals from GCaMP6f and PSTHs convolved with the GCaMP6s kernel. Boxplots show correlations between retinal ganglion cell clusters and wide-field neuron clusters.

(F) Example retinal ganglion cells identified by molecular labeling, stratification profile, dendritic tree size, and visual responses. Data as in Figure 2.

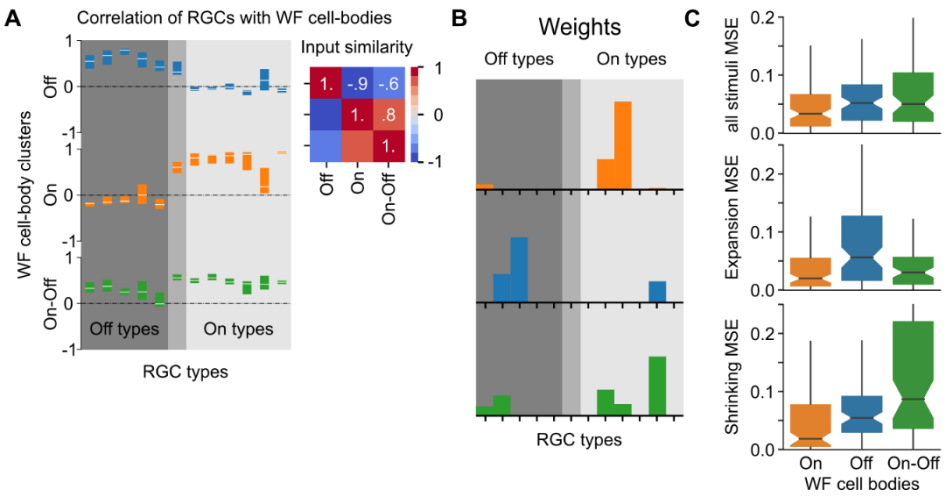

Figure S3. Contribution of Retinal Ganglion Cells to Wide-Field Neuron Signaling, Related to Figure 3.

(A) Correlation between retinal ganglion cell types and wide-field neuron subtypes. Boxplots show median and interquartile range.

(B) Fitted weights for predicting average wide-field neuron subtype responses.

(C) Mean squared error (MSE) of response reconstruction across wide-field neuron clusters. Boxplots show median, interquartile range, confidence interval of the median (nudges), and whiskers extending to 1.5× the interquartile range.

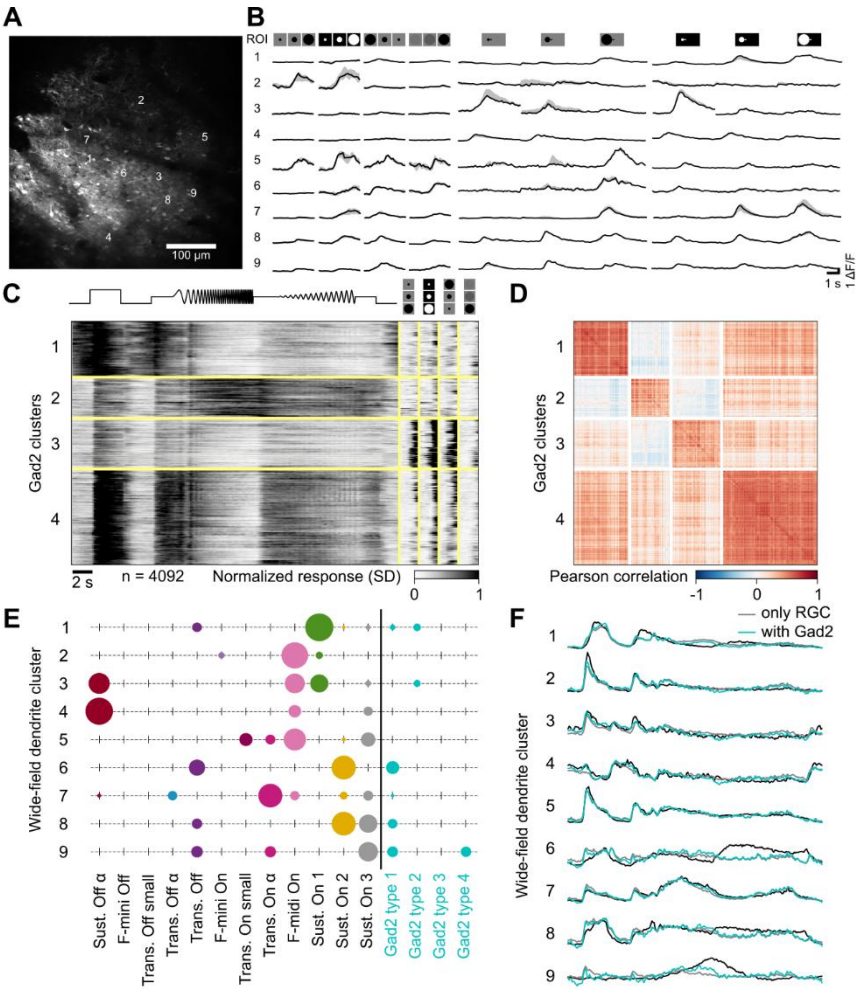

Figure S4. Clustering of Gad2 Neurons and Contribution to Responses of Wide-Field Neuron Dendrites, Related to Figure 4.

(A) Sample recording of Gad2 neurons in the colliculus.

(B) Median and interquartile range of calcium responses of cells indicated in (A).

(C) Heatmap of normalized and clustered responses to full-field, expanding, shrinking and dimming stimuli.

(D) Correlation matrix of cell responses in (C).

(E) Weights of the non-negative linear fit of wide-field dendrite responses including Gad2 neurons.

(F) Mean wide-field dendrite responses (black) and fits with/without Gad2 neurons (cyan/gray).

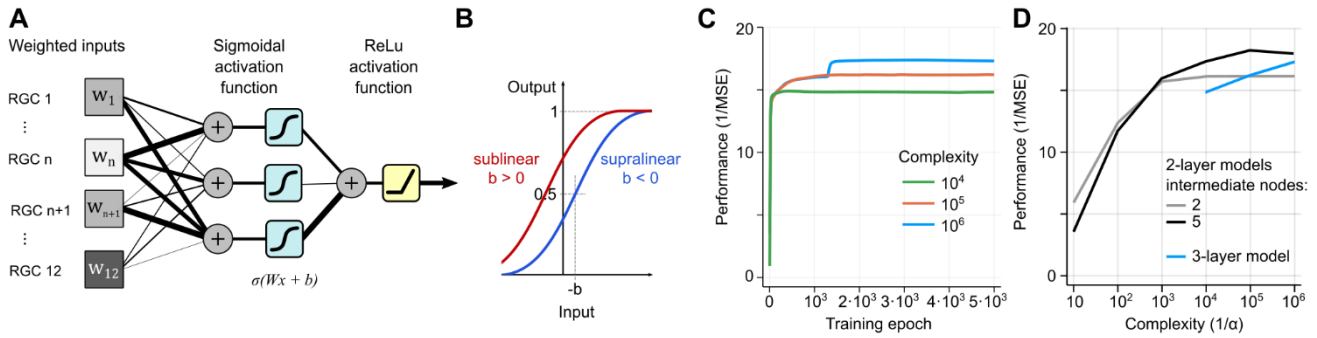

Figure S5. Training of the Multilayer Perceptron and Model Performance by Complexity, Related to Figure 5.

(A) Architecture of the multilayer perceptron (MLP) model, consisting of two layers with three hidden nodes using sigmoidal activation functions and a single output node with a rectifying nonlinearity. The model pools inputs from twelve weighted retinal ganglion cell types.

(B) Sigmoidal nonlinearity with positive and negative bias terms (b), accounting for supralinear and sublinear integration of inputs, respectively.

(C) Model performance during training tested on withheld data. Model parameters (weights W and biases b) are regularized using an L1 cost function scaled by α, controlling the trade-off between model complexity and performance. Model complexity is inversely proportional to α (1/α), while performance is evaluated as the inverse of the mean squared error (1/MSE). Only models with high complexity outperform linear models.

(D) Model performance by complexity for different 2-layer and 3-layer models.

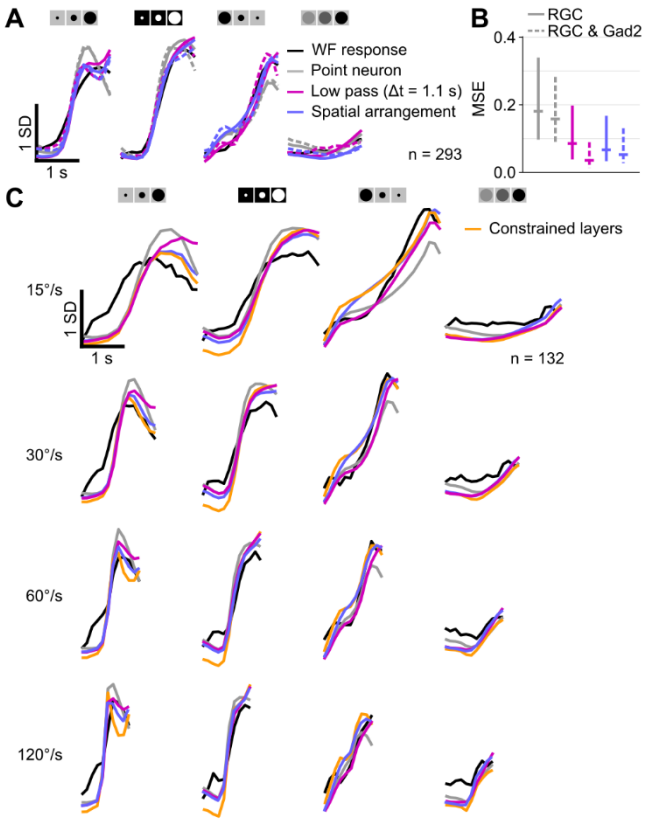

Figure S6. Comparison between different linear fits of wide-field neuron responses, Related to Figure 6 and 7.

(C) Average wide-field neuron responses to expanding, shrinking and dimming disks and linear model fits: point neuron (gray), low pass filter model with 1.1 s delay (magenta), and spatial arrangement model (purple). Fitted weights of retinal ganglion cells alone (RGC, solid lines) or retinal ganglion cells and Gad2+ neurons of the colliculus (RGC & Gad2, dashed lines). Data from 293 wide-field neurons.

(B) Mean squared error (MSE) of fits in (A). Horizontal and vertical lines indicate median and interquartile range.

(C) Average wide-field neuron responses to expanding, shrinking and dimming disks of 15, 30, 60 and 120°/s edge speed (top to bottom) and linear model fits: point neuron (gray), low pass filter model with 1.1 s delay (magenta), spatial arrangement (purple) and with constrained layers (orange). Data from 132 wide-field neurons.